EUROPEAN LABORATORY FOR PARTICLE PHYSICS

Measurement of the Strong Coupling Constant $\alpha_{\rm s}$ and the Vector and Axial-Vector Spectral Functions in Hadronic Tau Decays

The OPAL Collaboration

Abstract

The spectral functions of the vector current and the axial-vector current have been measured in hadronic τ decays using the OPAL detector at LEP. Within the framework of the Operator Product Expansion a simultaneous determination of the strong coupling constant $\alpha_{\rm s}$, the non-perturbative operators of dimension 6 and 8 and of the gluon condensate has been performed. Different perturbative descriptions have been compared to the data. The Contour Improved Fixed Order Perturbation Theory gives $\alpha_{\rm s}(m_\tau^2) = 0.348 \pm 0.009_{\rm exp} \pm 0.019_{\rm theo}$ at the τ-mass scale and $\alpha_{\rm s}(m_{\rm Z}^2) = 0.1219 \pm 0.0010_{\rm exp} \pm 0.0017_{\rm theo}$ at the Z^0-mass scale. The values obtained for $\alpha_{\rm s}(m_{\rm Z}^2)$ using Fixed Order Perturbation Theory or Renormalon Chain Resummation are 2.3 % and 4.1 % smaller, respectively. The 'running' of the strong coupling between $s_0 \simeq 1.3\,{\rm GeV}^2$ and $s_0 = m_\tau^2$ has been tested from direct fits to the integrated differential hadronic decay rate $R_\tau(s_0)$. A test of the saturation of QCD sum rules at the τ-mass scale has been performed.

The OPAL Collaboration

K. Ackerstaff[8], G. Alexander[23], J. Allison[16], N. Altekamp[5], K.J. Anderson[9], S. Anderson[12], S. Arcelli[2], S. Asai[24], S.F. Ashby[1], D. Axen[29], G. Azuelos[18,a], A.H. Ball[17], E. Barberio[8], R.J. Barlow[16], R. Bartoldus[3], J.R. Batley[5], S. Baumann[3], J. Bechtluft[14], T. Behnke[8], K.W. Bell[20], G. Bella[23], S. Bentvelsen[8], S. Bethke[14], S. Betts[15], O. Biebel[14], A. Biguzzi[5], S.D. Bird[16], V. Blobel[27], I.J. Bloodworth[1], M. Bobinski[10], P. Bock[11], J. Böhme[14], M. Boutemeur[34], S. Braibant[8], P. Bright-Thomas[1], R.M. Brown[20], H.J. Burckhart[8], C. Burgard[8], R. Bürgin[10], P. Capiluppi[2], R.K. Carnegie[6], A.A. Carter[13], J.R. Carter[5], C.Y. Chang[17], D.G. Charlton[1,b], D. Chrisman[4], C. Ciocca[2], P.E.L. Clarke[15], E. Clay[15], I. Cohen[23], J.E. Conboy[15], O.C. Cooke[8], C. Couyoumtzelis[13], R.L. Coxe[9], M. Cuffiani[2], S. Dado[22], G.M. Dallavalle[2], R. Davis[30], S. De Jong[12], L.A. del Pozo[4], A. de Roeck[8], K. Desch[8], B. Dienes[33,d], M.S. Dixit[7], M. Doucet[18], J. Dubbert[34], E. Duchovni[26], G. Duckeck[34], I.P. Duerdoth[16], D. Eatough[16], P.G. Estabrooks[6], E. Etzion[23], H.G. Evans[9], F. Fabbri[2], A. Fanfani[2], M. Fanti[2], A.A. Faust[30], F. Fiedler[27], M. Fierro[2], H.M. Fischer[3], I. Fleck[8], R. Folman[26], A. Fürtjes[8], D.I. Futyan[16], P. Gagnon[7], J.W. Gary[4], J. Gascon[18], S.M. Gascon-Shotkin[17], C. Geich-Gimbel[3], T. Geralis[20], G. Giacomelli[2], P. Giacomelli[2], V. Gibson[5], W.R. Gibson[13], D.M. Gingrich[30,a], D. Glenzinski[9], J. Goldberg[22], W. Gorn[4], C. Grandi[2], E. Gross[26], J. Grunhaus[23], M. Gruwé[27], G.G. Hanson[12], M. Hansroul[8], M. Hapke[13], C.K. Hargrove[7], C. Hartmann[3], M. Hauschild[8], C.M. Hawkes[5], R. Hawkings[27], R.J. Hemingway[6], M. Herndon[17], G. Herten[10], R.D. Heuer[8], M.D. Hildreth[8], J.C. Hill[5], S.J. Hillier[1], P.R. Hobson[25], A. Hocker[9], R.J. Homer[1], A.K. Honma[28,a], D. Horváth[32,c], K.R. Hossain[30], R. Howard[29], P. Hüntemeyer[27], P. Igo-Kemenes[11], D.C. Imrie[25], K. Ishii[24], F.R. Jacob[20], A. Jawahery[17], H. Jeremie[18], M. Jimack[1], A. Joly[18], C.R. Jones[5], P. Jovanovic[1], T.R. Junk[8], D. Karlen[6], V. Kartvelishvili[16], K. Kawagoe[24], T. Kawamoto[24], P.I. Kayal[30], R.K. Keeler[28], R.G. Kellogg[17], B.W. Kennedy[20], A. Klier[26], S. Kluth[8], T. Kobayashi[24], M. Kobel[3,e], D.S. Koetke[6], T.P. Kokott[3], M. Kolrep[10], S. Komamiya[24], R.V. Kowalewski[28], T. Kress[11], P. Krieger[6], J. von Krogh[11], P. Kyberd[13], G.D. Lafferty[16], D. Lanske[14], J. Lauber[15], S.R. Lautenschlager[31], I. Lawson[28], J.G. Layter[4], D. Lazic[22], A.M. Lee[31], E. Lefebvre[18], D. Lellouch[26], J. Letts[12], L. Levinson[26], R. Liebisch[11], B. List[8], C. Littlewood[5], A.W. Lloyd[1], S.L. Lloyd[13], F.K. Loebinger[16], G.D. Long[28], M.J. Losty[7], J. Ludwig[10], D. Liu[12], A. Macchiolo[2], A. Macpherson[30], M. Mannelli[8], S. Marcellini[2], C. Markopoulos[13], A.J. Martin[13], J.P. Martin[18], G. Martinez[17], T. Mashimo[24], P. Mättig[26], W.J. McDonald[30], J. McKenna[29], E.A. Mckigney[15], T.J. McMahon[1], R.A. McPherson[28], F. Meijers[8], S. Menke[3], F.S. Merritt[9], H. Mes[7], J. Meyer[27], A. Michelini[2], S. Mihara[24], G. Mikenberg[26], D.J. Miller[15], R. Mir[26], W. Mohr[10], A. Montanari[2], T. Mori[24], K. Nagai[26], I. Nakamura[24], H.A. Neal[12], B. Nellen[3], R. Nisius[8], S.W. O'Neale[1], F.G. Oakham[7], F. Odorici[2], H.O. Ogren[12], M.J. Oreglia[9], S. Orito[24], J. Pálinkás[33,d], G. Pásztor[32], J.R. Pater[16], G.N. Patrick[20], J. Patt[10], R. Perez-Ochoa[8], S. Petzold[27], P. Pfeifenschneider[14], J.E. Pilcher[9], J. Pinfold[30], D.E. Plane[8], P. Poffenberger[28], B. Poli[2], J. Polok[8], M. Przybycień[8], C. Rembser[8], H. Rick[8], S. Robertson[28], S.A. Robins[22], N. Rodning[30], J.M. Roney[28], K. Roscoe[16], A.M. Rossi[2], Y. Rozen[22], K. Runge[10], O. Runolfsson[8], D.R. Rust[12], K. Sachs[10], T. Saeki[24], O. Sahr[34], W.M. Sang[25], E.K.G. Sarkisyan[23], C. Sbarra[29], A.D. Schaile[34], O. Schaile[34], F. Scharf[3], P. Scharff-Hansen[8], J. Schieck[11], B. Schmitt[8], S. Schmitt[11], A. Schöning[8], T. Schorner[34], M. Schröder[8], M. Schumacher[3], C. Schwick[8], W.G. Scott[20], R. Seuster[14], T.G. Shears[8], B.C. Shen[4], C.H. Shepherd-Themistocleous[8], P. Sherwood[15], G.P. Siroli[2], A. Sittler[27], A. Skuja[17], A.M. Smith[8], G.A. Snow[17], R. Sobie[28],

S. Söldner-Rembold[10], M. Sproston[20], A. Stahl[3], K. Stephens[16], J. Steuerer[27], K. Stoll[10],
D. Strom[19], R. Ströhmer[34], R. Tafirout[18], S.D. Talbot[1], S. Tanaka[24], P. Taras[18], S. Tarem[22],
R. Teuscher[8], M. Thiergen[10], M.A. Thomson[8], E. von Törne[3], E. Torrence[8], S. Towers[6],
I. Trigger[18], Z. Trócsányi[33], E. Tsur[23], A.S. Turcot[9], M.F. Turner-Watson[8], R. Van Kooten[12],
P. Vannerem[10], M. Verzocchi[10], P. Vikas[18], H. Voss[3], F. Wäckerle[10], A. Wagner[27], C.P. Ward[5],
D.R. Ward[5], P.M. Watkins[1], A.T. Watson[1], N.K. Watson[1], P.S. Wells[8], N. Wermes[3],
J.S. White[28], G.W. Wilson[14], J.A. Wilson[1], T.R. Wyatt[16], S. Yamashita[24], G. Yekutieli[26],
V. Zacek[18], D. Zer-Zion[8]

[1]School of Physics and Astronomy, University of Birmingham, Birmingham B15 2TT, UK
[2]Dipartimento di Fisica dell' Università di Bologna and INFN, I-40126 Bologna, Italy
[3]Physikalisches Institut, Universität Bonn, D-53115 Bonn, Germany
[4]Department of Physics, University of California, Riverside CA 92521, USA
[5]Cavendish Laboratory, Cambridge CB3 0HE, UK
[6]Ottawa-Carleton Institute for Physics, Department of Physics, Carleton University, Ottawa, Ontario K1S 5B6, Canada
[7]Centre for Research in Particle Physics, Carleton University, Ottawa, Ontario K1S 5B6, Canada
[8]CERN, European Organisation for Particle Physics, CH-1211 Geneva 23, Switzerland
[9]Enrico Fermi Institute and Department of Physics, University of Chicago, Chicago IL 60637, USA
[10]Fakultät für Physik, Albert Ludwigs Universität, D-79104 Freiburg, Germany
[11]Physikalisches Institut, Universität Heidelberg, D-69120 Heidelberg, Germany
[12]Indiana University, Department of Physics, Swain Hall West 117, Bloomington IN 47405, USA
[13]Queen Mary and Westfield College, University of London, London E1 4NS, UK
[14]Technische Hochschule Aachen, III Physikalisches Institut, Sommerfeldstrasse 26-28, D-52056 Aachen, Germany
[15]University College London, London WC1E 6BT, UK
[16]Department of Physics, Schuster Laboratory, The University, Manchester M13 9PL, UK
[17]Department of Physics, University of Maryland, College Park, MD 20742, USA
[18]Laboratoire de Physique Nucléaire, Université de Montréal, Montréal, Quebec H3C 3J7, Canada
[19]University of Oregon, Department of Physics, Eugene OR 97403, USA
[20]Rutherford Appleton Laboratory, Chilton, Didcot, Oxfordshire OX11 0QX, UK
[22]Department of Physics, Technion-Israel Institute of Technology, Haifa 32000, Israel
[23]Department of Physics and Astronomy, Tel Aviv University, Tel Aviv 69978, Israel
[24]International Centre for Elementary Particle Physics and Department of Physics, University of Tokyo, Tokyo 113, and Kobe University, Kobe 657, Japan
[25]Institute of Physical and Environmental Sciences, Brunel University, Uxbridge, Middlesex UB8 3PH, UK
[26]Particle Physics Department, Weizmann Institute of Science, Rehovot 76100, Israel
[27]Universität Hamburg/DESY, II Institut für Experimental Physik, Notkestrasse 85, D-22607 Hamburg, Germany
[28]University of Victoria, Department of Physics, P O Box 3055, Victoria BC V8W 3P6, Canada
[29]University of British Columbia, Department of Physics, Vancouver BC V6T 1Z1, Canada

[30]University of Alberta, Department of Physics, Edmonton AB T6G 2J1, Canada
[31]Duke University, Dept of Physics, Durham, NC 27708-0305, USA
[32]Research Institute for Particle and Nuclear Physics, H-1525 Budapest, P O Box 49, Hungary
[33]Institute of Nuclear Research, H-4001 Debrecen, P O Box 51, Hungary
[34]Ludwigs-Maximilians-Universität München, Sektion Physik, Am Coulombwall 1, D-85748 Garching, Germany

[a] and at TRIUMF, Vancouver, Canada V6T 2A3
[b] and Royal Society University Research Fellow
[c] and Institute of Nuclear Research, Debrecen, Hungary
[d] and Department of Experimental Physics, Lajos Kossuth University, Debrecen, Hungary
[e] on leave of absence from the University of Freiburg

1   Introduction

The τ lepton is the only lepton heavy enough to decay into hadrons. A comparison of the inclusive hadronic decay rate of the τ with QCD predictions can give fundamental parameters of the theory. The energy regime governed by $m_\tau = 1.777\,\mathrm{GeV}$ is regarded as a compromise region between the low and high energy regimes where non-perturbative and perturbative QCD dominate, respectively. In fact, τ decay is probably the lowest-energy process from which the coupling constant α_s can be cleanly extracted [1–5] without large complications from non-perturbative effects, while the perturbative expansion still converges well.

In this analysis the most important quantity to measure is the strong coupling constant $\alpha_\mathrm{s}(m_\tau^2)$. The 'running' of α_s, for energy scales smaller than m_τ, can be tested with the integrated differential decay rate into hadrons $\mathrm{d}R_\tau/\mathrm{d}s$, where $\sqrt{s}$ denotes the mass of the final-state hadronic system and $R_\tau = \Gamma(\tau \to \mathrm{h}\nu_\tau)/\Gamma(\tau \to \mathrm{e}\nu_\mathrm{e}\nu_\tau)$ is the hadronic decay width of the tau normalized to the decay width of the tau going into electron and neutrinos. This is possible as the hadronic decay rate $R_\tau(s_0)$ depends on the strong coupling constant $\alpha_\mathrm{s}(s_0)$ at the scale s_0 only, where s_0 denotes the upper integration limit for the integral over $\mathrm{d}R_\tau/\mathrm{d}s$.

The measured $\alpha_\mathrm{s}(m_\tau^2)$ can be transformed into a value for $\alpha_\mathrm{s}(m_\mathrm{Z}^2)$ through the renormalization group equation (β-function). In doing that, the relative error of $\alpha_\mathrm{s}(s)$ decreases like the decrease of $\alpha_\mathrm{s}(s)$ itself. After the evolution to the Z^0 mass the strong coupling is reduced to $\alpha_\mathrm{s}(m_\mathrm{Z}^2) \simeq (1/3)\alpha_\mathrm{s}(m_\tau^2)$ and its error is reduced to $\Delta\alpha_\mathrm{s}(m_\mathrm{Z}^2) \simeq (1/9)\Delta\alpha_\mathrm{s}(m_\tau^2)$. Hence, the significance of this measurement compares favorably with other $\alpha_\mathrm{s}(m_\mathrm{Z}^2)$ determination methods [6].

Inclusive observables like the hadronic decay rate $R_\tau(s_0)$ have been calculated in perturbative QCD to $O(\alpha_\mathrm{s}^3)$. Some remaining theoretical uncertainties due to corrections in powers of $1/m_\tau^2$ can be avoided if the differential decay rate $\mathrm{d}R_\tau/\mathrm{d}s$ is measured and compared to the theory by means of its spectral moments which are weighted integrals over $\mathrm{d}R_\tau/\mathrm{d}s$. As a result, the power corrections and α_s can be simultaneously determined from a fit. While $R_\tau(m_\tau^2)$ can be precisely determined from the leptonic branching ratios and the τ lifetime, $\mathrm{d}R_\tau/\mathrm{d}s$ involves a measurement of the invariant mass of the hadronic system. Thus, an exclusive reconstruction of all hadronic final states in τ decays is necessary.

In this paper an analysis is presented using data taken with the OPAL detector at LEP at energies within $\pm 3\,\mathrm{GeV}$ of the Z^0 peak. The analysis includes measurements of the differential decay rates $\mathrm{d}R_{\tau,\mathrm{V/A}}/\mathrm{d}s$ for vector (V) and axial-vector (A) decays and their respective spectral moments. Using these moments, fits of QCD predictions are made extracting the strong coupling constant $\alpha_\mathrm{s}(m_\tau^2)$ and parameters of the non-perturbative expansion, most notably the contributions of dimension 6 and 8 operators. The measurement is based on a set of spectral moments defined by the same weighting functions used by ALEPH [7, 8] and CLEO [9].

The differential decay rates themselves can be re-expressed in terms of spectral functions of the vector and axial-vector current, $v(s)$ and $a(s)$. This measurement serves for saturation tests of QCD sum rules at the τ-mass scale by comparing the experimental values of the sum rules with chiral QCD predictions. Furthermore, by evaluating the moment integrals between zero and s_0, where $\sqrt{s_0}$ is an energy smaller than m_τ, the 'running' of α_s is tested in a single experiment.

The theoretical framework for inclusive observables from hadronic τ decays is described in section 2. After a short description of the OPAL detector in section 3 the selection of hadronic τ decays is described in section 4. In section 5 the unfolding procedure is described. The measured and unfolded spectra are discussed in section 6 followed by a description of the systematic uncertainties in section 7. Section 8 contains the results for the moments of R_τ and

for the spectral functions. The extraction of the strong coupling constant and of the power corrections, from fits to the moments of $R_\tau(s_0)$, is discussed in sections 9 and 10. Section 11 describes the test of the 'running' of α_s. The application of QCD sum rules to the spectral functions is discussed in section 12. Finally, the results are summarized in section 13.

2   Theoretical description of hadronic τ decays

QCD predictions of inclusive observables in hadronic τ decays have been calculated including perturbative and non-perturbative contributions. These observables can be related to the differential, non-strange hadronic decay width, normalized to the decay width of $\tau^- \to e^- \overline{\nu}_e \nu_\tau$ [1–5]:

$$\frac{\mathrm{d}R_{\tau,\mathrm{V/A}}}{\mathrm{d}s} = 12\pi S_{\mathrm{EW}}|V_{\mathrm{ud}}|^2 \frac{1}{m_\tau^2} \left(1 - \frac{s}{m_\tau^2}\right)^2 \left[\left(1 + 2\frac{s}{m_\tau^2}\right) \mathrm{Im}\Pi_{\mathrm{V/A}}^{(1)}(s) + \mathrm{Im}\Pi_{\mathrm{V/A}}^{(0)}(s)\right], \quad (1)$$

where s denotes the square of the invariant mass of the hadronic system and the labels V and A stand for the vector and axial-vector contributions, respectively[1]. $S_{\mathrm{EW}} = 1.0194$ is an electroweak correction term [10] and $|V_{\mathrm{ud}}|^2 = 0.9512 \pm 0.0008$ is the squared CKM weak mixing matrix element [11]. The functions $\mathrm{Im}\Pi$ are proportional to the spectral functions for the non-strange currents with angular momenta $J = 1$ and $J = 0$ as indicated by the superscripts. The latter spectral function vanishes for the vector current, since no scalar particle has been observed in τ decays, while $\mathrm{Im}\Pi_{\mathrm{A}}^0$ is given by the pion pole, assuming that the pion is the only pseudo-scalar final-state in non-strange τ decays:

$$\mathrm{Im}\Pi_{\mathrm{A}}^0(s) = \frac{m_\tau^2}{12\pi S_{\mathrm{EW}}|V_{\mathrm{ud}}|^2} \left(1 - \frac{s}{m_\tau^2}\right)^{-2} \frac{B(\tau \to \pi\nu_\tau)}{B(\tau \to e\nu_e\nu_\tau)} \frac{1}{N_\pi} \frac{\mathrm{d}N_\pi}{\mathrm{d}s}, \quad (2)$$

with N_π being the number of selected τ decays into pions. The spectral functions for the vector and the axial-vector currents are defined in equation (22).

Within the framework of QCD weighted integrals or moments of (1) have been calculated [12]:

$$R_{\tau,\mathrm{V/A}}^{kl}(s_0) = \int_0^{s_0} \mathrm{d}s \left(1 - \frac{s}{s_0}\right)^k \left(\frac{s}{m_\tau^2}\right)^l \frac{\mathrm{d}R_{\tau,\mathrm{V/A}}}{\mathrm{d}s}. \quad (3)$$

The moments are used to compare the experiment with theory. In what follows, ten moments for $kl = 00, 10, 11, 12, 13$ for V and A are used. The first moments $R_{\tau,\mathrm{V/A}}^{00}(m_\tau^2)$ are the total normalized decay rates of the τ into vector and axial-vector mesons given by (1) integrated over s. In the naïve parton model these two rates are identical and add up to the number of colors. Since only non-strange currents are considered in this work the naïve expectation has to be multiplied by $|V_{\mathrm{ud}}|^2$. Including the perturbative and non-perturbative contributions, equation (3) is usually written as [12]:

$$R_{\tau,\mathrm{V/A}}^{kl}(s_0) = \frac{3}{2} S_{\mathrm{EW}}|V_{\mathrm{ud}}|^2 \left(1 + \delta_{\mathrm{EW}}^{\prime kl}(s_0) + \delta_{\mathrm{pert}}^{kl}(s_0) + \sum_{D=2,4,6,\ldots} \delta_{\mathrm{V/A}}^{D,kl}(s_0)\right), \quad (4)$$

where S_{EW} is the same multiplicative correction as in equation (1) and $\delta_{\mathrm{EW}}^{\prime kl}$ are additive electroweak corrections. The latter has been calculated for $kl = 00$ only [13] yielding $\delta_{\mathrm{EW}}^{\prime 00}(m_\tau^2) =$

---

[1]The notation V/A will be used throughout the paper to indicate vector and axial-vector contributions, respectively.

$\frac{5}{12}\frac{\alpha(m_\tau^2)}{\pi} = 0.0010$. In the higher moments it is assumed that this term scales with the integral over the weight functions in equations (1) and (3) like the $O(\alpha_s)$ correction:

$$\delta_{\text{EW}}'^{kl}(s_0) = \frac{R_{\tau,\text{naïve}}^{kl}(s_0)}{R_{\tau,\text{naïve}}^{00}(m_\tau^2)}\delta_{\text{EW}}'^{00}(m_\tau^2). \tag{5}$$

Therefore the $\delta_{\text{EW}}'^{kl}$ contribution to the moments is small ($\sim 0.1\,\%$) and the uncertainty due to this term is neglected in the analysis. The other factors in equation (4) are explained in more detail below.

2.1 Perturbative correction terms $\delta_{\text{pert}}^{kl}$

The perturbative term $\delta_{\text{pert}}^{kl}$ is known to third order in α_s [4] and partly known to fourth order in α_s [12]. For $kl = 00$ and $s_0 = m_\tau^2$ it is:

$$\delta_{\text{pert}}^{00}(m_\tau^2) = \frac{\alpha_s(m_\tau^2)}{\pi} + 5.2023\frac{\alpha_s^2(m_\tau^2)}{\pi^2} + 26.366\frac{\alpha_s^3(m_\tau^2)}{\pi^3} + (78.003 + K_4)\frac{\alpha_s^4(m_\tau^2)}{\pi^4} + O\left(\alpha_s^5(m_\tau^2)\right). \tag{6}$$

This result which truncates after the fourth power of α_s is refered to as Fixed Order Perturbation Theory (FOPT). Different attempts have been made to obtain a resummation of some of the higher order terms. The resummation scheme proposed in [12] compensates for higher order logarithmic terms in α_s by expressing the $\delta_{\text{pert}}^{kl}(s_0)$ terms by contour-integrals in the complex s-plane along the circle $|s| = s_0$ and solving numerically for each $\alpha_s(s)$ along the circle (Contour-Improved Perturbation Theory, CIPT). The different $\alpha_s(s)$ values on the circle can be calculated from $\alpha_s(m_\tau^2)$ by solving numerically the β-function:

$$\frac{da}{d\ln s} = \beta(a) = -\beta_1 a^2 - \beta_2 a^3 - \beta_3 a^4 - \beta_4 a^5 + O(a^6), \tag{7}$$

with $a = \alpha_s(s)/\pi$, $\beta_1 = 9/4$, $\beta_2 = 4$, $\beta_3^{\overline{\text{MS}}} = 10.0599$ and $\beta_4^{\overline{\text{MS}}} = 47.2306$ [14] for 3 quark flavors. The last two coefficients are renormalization scheme dependent and the quoted values belong to the $\overline{\text{MS}}$-scheme. The third method considered in this paper resums the leading term of the β-function to all orders in α_s by inserting so-called Renormalon Chains (RCPT) [15–17][2].

One of the leading theoretical uncertainties for FOPT and CIPT comes from the unknown $O(\alpha_s^4)$ correction K_4. Expanding the perturbative corrections in terms of CIPT gives:

$$1 + \delta_{\text{pert}}^{kl}(s_0) = \sum_{n\geq 0} K_n A_n^{kl}(s_0), \tag{8}$$

where the functions A_n^{kl} are the weighted contour integrals. For $kl = 00$ the function is:

$$A_n^{00}(s_0) = \frac{1}{2\pi i}\oint_{|s|=s_0}\frac{ds}{s}\left(\frac{\alpha_s(-s)}{\pi}\right)^n\left(2\frac{s_0}{m_\tau^2} - 2\frac{s_0^3}{m_\tau^6} + \frac{s_0^4}{m_\tau^8} - 2\frac{s}{m_\tau^2} + 2\frac{s^3}{m_\tau^6} - \frac{s^4}{m_\tau^8}\right). \tag{9}$$

In the $\overline{\text{MS}}$-scheme and for three flavors the first four terms are: $K_0 = K_1 = 1$, $K_2 = 1.63982$, $K_3 = 6.37101$ [18–22]. A bold guess for K_4 gives $K_4 \approx K_3(K_3/K_2) \approx 25$ [12]. Similar estimates are given in [23, 24]. A central value of $K_4 = 25$ is used, with an uncertainty of $\Delta K_4 = \pm 50$ in the perturbative expansions for CIPT and FOPT.

---

[2]The fixed-order corrected version (up to the third order in α_s) quoted in the lower portion of table 6 in ref. [15] is used in the fit.

Another major theoretical uncertainty is the choice of renormalization scale μ in the α_s dependence of $\delta_{\text{pert}}^{kl}(s_0)$. The scale ratio $\zeta = \mu^2/s_0$ is varied from 0.4 to 2.0 in all three models described above as suggested in [5].

The choice of the renormalization scheme (RS) can also alter the result. Following the prescription in [5] the third coefficient of the β-function β_3^{RS} is varied between 0.0 and 2.0 $\beta_3^{\overline{\text{MS}}}$ in order to obtain the uncertainty due to different renormalization schemes.

2.2 Power correction terms $\delta_{\text{V/A}}^{D,kl}$

In the framework of the Operator Product Expansion (OPE) [25] the non-perturbative contributions are expressed as a power series in terms of $1/m_\tau^2$ absorbing the long-distance dynamics into vacuum matrix elements $\langle \mathcal{O}(\tilde{\mu}) \rangle$ [4, 26–28]. Thus, they can be written as sums over power corrections of different dimensions, D:

$$\delta_{\text{non-pert,V/A}}^{kl}(s_0) = \sum_{D=2,4,6,\ldots} \delta_{\text{V/A}}^{D,kl}(s_0). \tag{10}$$

In contrast to the perturbative part described in the previous section the power corrections differ for the vector and the axial-vector currents.

In equation (10) the correction of dimension $D = 2$ is a mass correction term and therefore belongs to the perturbative part. The $D = 4$ term is the first term with major non-perturbative contributions, namely the quark condensates for the three light flavors $\langle \overline{\psi}\psi \rangle_{\text{u,d,s}}$ and the gluon condensate $\langle \frac{\alpha_s}{\pi} GG \rangle$. If one neglects the small s-dependence of the power corrections, the $\delta_{\text{V/A}}^{D,kl}$ terms can be expressed for all kl values by a product of the same (vector/axial-vector) operator of dimension D (or the power correction for $kl = 00$) and a simple integral over the kl-dependent weight-functions [12]:

$$
\delta_{\text{V/A}}^{D,kl}(s_0) = 8\pi^2
\begin{array}{ccccc}
{\scriptstyle D=2} & {\scriptstyle D=4} & {\scriptstyle D=6} & {\scriptstyle D=8} & {\scriptstyle D=10} \\
\end{array}
\begin{pmatrix}
1 & 0 & -3 & -2 & 0 \\
1 & \frac{m_\tau^2}{s_0} & -3 & -2 - 3\frac{m_\tau^2}{s_0} & -2\frac{m_\tau^2}{s_0} \\
0 & -1 & -\frac{m_\tau^2}{s_0} & 3 & 2 + 3\frac{m_\tau^2}{s_0} \\
0 & 0 & 1 & \frac{m_\tau^2}{s_0} & -3 \\
0 & 0 & 0 & -1 & -\frac{m_\tau^2}{s_0}
\end{pmatrix}
\begin{array}{c}
{\scriptstyle kl} \\
{\scriptstyle 00} \\
{\scriptstyle 10} \\
{\scriptstyle 11} \\
{\scriptstyle 12} \\
{\scriptstyle 13}
\end{array}
\tag{11}
$$
$$
\times \sum_{\dim \mathcal{O} = D} \frac{\mathcal{C}_{\text{V/A}}(\tilde{\mu}) \langle \mathcal{O}(\tilde{\mu}) \rangle}{m_\tau^D},
$$

where each entry in the matrix belongs to a particular dimension D and a particular moment kl, as denoted by the first row and the last column. The parameter $\tilde{\mu}$ is an arbitrary factorization scale which separates the long-distance non-perturbative effects, which are absorbed in the vacuum matrix elements $\langle \mathcal{O}(\tilde{\mu}) \rangle$, from short-distance perturbative effects which are incorporated in the Wilson coefficients $\mathcal{C}_{\text{V/A}}(\tilde{\mu})$ [12].

This approach is used for the dimension $D = 6$ and $D = 8$ terms, taking $\delta_{\text{V/A}}^{6/8,00}$ as free parameters. For the dimension $D = 2$ and $D = 4$ terms the full s-dependence is taken into account for the theoretical description of the moments [12]. The least precisely known $D = 4$ parameter, the gluon condensate, which is known only to 50 % [4], is also taken as a free parameter in the fit, while the $D = 2$ term is calculated from the quark masses and the strong coupling.

Terms with dimensions higher then 8 are neglected in this analysis as they do not contribute to $R_{\tau,\text{V/A}}^{00}$ as can be seen from equation (11).

7

3 OPAL detector

A detailed description of the OPAL detector can be found in [29]. A brief description of the features relevant for this analysis follows.

A high-precision silicon microvertex detector surrounds the beam pipe. It covers the angular region of $|\cos\theta| \leq 0.8$ and provides tracking information in the r-φ (and z after 1992) directions[3] [30, 31]. Charged particles are tracked in a central detector enclosed inside a solenoid that provides a uniform axial magnetic field of 0.435 T. The central detector consists of three drift chambers: a high-resolution vertex detector, the large-volume jet chamber and the z-chambers. The jet chamber records the momentum and energy loss of charged particles over 98 % of the solid angle and the z-chambers are used to improve the track position measurement in the z direction [32].

Outside the solenoid coil are scintillation counters which measure the time-of-flight from the interaction region and aid in the rejection of cosmic events. Next is the electromagnetic calorimeter (ECAL) that is divided into a barrel ($|\cos\theta| < 0.82$) and two endcap ($0.81 < |\cos\theta| < 0.98$) sections. The barrel section is composed of 9440 lead-glass blocks pointing to the interaction region. Each block subtends approximately $10 \times 10 \, \text{cm}^2$ with a depth of 24.6 radiation lengths. The two endcap sections consist of dome-shaped arrays, each having 1132 lead-glass blocks, mounted coaxial with the beam, where each block covers $9.2 \times 9.2 \, \text{cm}^2$ with a typical depth of 22 radiation lengths. The hadron calorimeter (HCAL) is beyond the electromagnetic calorimeter and instrumented with layers of limited streamer tubes in the iron of the solenoid magnet return yoke. In the region $|\cos\theta| < 0.81$ this detector typically has a depth of 8 interaction lengths. The hadron calorimeter is covered by the muon chamber system, composed of four layers of drift chambers in the barrel region and four layers of limited streamer tubes in the endcap region.

4 Event selection and reconstruction of τ decays

OPAL data collected from 1990 to 1995 is used in this analysis. The data were taken within $\pm 3 \, \text{GeV}$ of the Z^0 resonance. The Monte Carlo samples used in this analysis consist of 600 000 τ-pair events generated at $\sqrt{s} = m_Z$ with KORALZ 4.0 [33]. Their decays were modelled with TAUOLA 2.4 [34] and then processed through the GEANT [35] OPAL detector simulation [36]. The non-τ background Monte Carlo samples consist of 1 000 000 $q\bar{q}$ events generated with JETSET 7.4 [37], 800 000 Bhabha events generated with RADBAB 2.0 [38,39], 600 000 μ-pair events generated with KORALZ 4.0 [33] and 800 000 events from two-photon processes generated with VERMASEREN 1.01 [40,41].

4.1 Selection of τ-lepton candidates

The standard τ selection procedure as described in [42] begins with the rejection of cosmic rays, multi-hadronic events and events from two-photon processes. Cosmic rays are rejected by the time-of-flight information of the tracks. Multihadrons are removed from the sample by requiring two narrow jets (cones with a half opening angle of 35°) and up to six tracks in the event. The events from two-photon processes are eliminated by allowing an acollinearity angle of up to 15° between the two jets.

---

[3] In the OPAL coordinate system the x-axis is horizontal and points to the center of LEP. The y-axis is vertical and the z-axis is in the e$^-$ beam direction. The angle θ is defined relative to the z-axis.

The remaining event sample contains tau pairs, Bhabha events, and muon pairs. Events with an energy deposit of more than $0.8 \times 2E_{\mathrm{beam}}$ are identified as Bhabhas. An event is classified as a muon pair if two tracks carry energy of more than $0.6 \times 2E_{\mathrm{beam}}$ and if both tracks have at least two hits in the muon chambers and almost no energy deposit in the ECAL. The remaining events are classified as τ pairs if the polar angle of the total cone momentum calculated from track momenta and ECAL clusters satisfies $|\cos\theta| < 0.95$ for both cones.

After this selection both cones in each event are treated independently. The non-tau background is further reduced by requiring one or three tracks in each cone with a total charge of plus or minus one. A total of 297 988 τ candidates survive these selection criteria with an estimated non-τ background fraction of 3.9 %.

4.2 Identification of τ-decay modes

A Maximum Likelihood selection as used in previous publications (see e.g. [43]) is applied to the data and the Monte Carlo samples to distinguish between the following decay modes: $\tau^- \rightarrow \nu_\tau X^-$, where X^- is one of $e^-\overline{\nu}_e$, $\mu^-\overline{\nu}_\mu$, π^-, $\pi^-\pi^0$, $\pi^-2\pi^0$, $\pi^-3\pi^0$, $2\pi^-\pi^+$, $2\pi^-\pi^+\pi^0$, $2\pi^-\pi^+2\pi^0$. The charge and parity conjugated modes are implicitly assumed for $\tau^+ \rightarrow \overline{\nu}_\tau X^+$ decays. Fourteen reference distributions are used to distinguish between the different one-prong channels and five reference distributions are used in the three-prong case. Decays with charged kaons instead of pions are suppressed by a cut on the specific energy loss $\mathrm{d}E/\mathrm{d}x$ in the drift chamber. Decays into electrons are distinguished from the other modes by the ratio E/p of the ECAL energy associated with the cone over the track momentum, and the $\mathrm{d}E/\mathrm{d}x$ information. Muons are identified by the number of hits in the muon chambers and the outermost HCAL layers. The different hadronic decay modes with zero, one, two or three neutral pions are separated by using the number of reconstructed photons in the ECAL (see section 4.3).

The decay channels used in this analysis are the three non-strange one-prong modes with at least one neutral pion: $\pi\pi^0$, $\pi2\pi^0$ and $\pi3\pi^0$, and the three non-strange three-prong modes: 3π, $3\pi\pi^0$, $3\pi2\pi^0$. A total of 65899 τ candidates are selected[4] in these channels with an estimated background fraction of 26.6 % including misidentified τ decays and the remaining non-τ background fraction of 0.8 %. Details about the treatment of the cross-talk between the signal channels due to misidentified τ decays are subject to sections 5 and 6.

The most important observable for the discrimination between vector and axial-vector channels is the number of neutral pions in a cone. A new method to reconstruct neutral pions in τ decays has been employed, which is described in the following section.

4.3 Reconstruction of neutral pions

Neutral pions are identified by their decay into two photons. Since photons are only detected in the ECAL, an iterative fit of photon energies and directions to the observed energy deposits in the ECAL blocks is performed.

The energy deposition in an ECAL block can be expressed as a function of the photon energy and the photon direction. This is done by parameterizing the integrated energy density of an electromagnetic shower for each ECAL block. In the barrel region of the ECAL where the blocks have a quasi-pointing geometry only lateral shower profiles need to be parameterized. They can be approximated by the sum of two exponential distributions representing core and

---

[4]For the decay mode $\pi\pi^0$ a cut on $|\cos\theta| < 0.9$ is used in order to reduce the background from Bhabha events.

halo components [44]. For the endcap region, where the blocks are oriented parallel to the beam, lateral and longitudinal profiles are important. The longitudinal profile is reasonably described by the gamma distribution [11].

The mean energy deposit of a minimum ionizing particle is subtracted from all ECAL blocks hit by a charged particle. The fit then finds the smallest number of photons needed to explain the measured energies and provides their corresponding three-vectors.

Energy depositions from hadronic interactions of charged pions in the ECAL are accounted for by assigning photon candidates which are close to track intersections with the ECAL to the track. The maximum angle allowed between a photon candidate and a track to which the photon candidate can be assigned depends on the polar angle of the track and varies between $1.2°$ and $1.7°$ in the barrel region and between $2.0°$ and $3.4°$ in the endcap region. A photon candidate close to a track is still classified as a photon if the total energy of photon candidates assigned to this track exceeds the measured track momentum.

All possible two-photon combinations are then used to find π^0 candidates. The combination resulting in the largest number of π^0 candidates with an average invariant mass deviation from the π^0 mass less than $1.5\,\sigma$ is selected. The error on the invariant two-photon mass, σ, is calculated from the error matrices of the above photon fit. The π^0 four-momenta are then calculated from the energies and directions of the photon pairs of the selected combination after a constrained fit to the π^0 mass. Figure 1 shows the photon-pair mass for selected $\pi\pi^0$ candidates before the π^0-mass constraint.

For all the one-prong modes a minimum energy of $0.7\,\text{GeV}$ for each reconstructed π^0 is required while $E_{\pi^0} > 2.0\,\text{GeV}$ is required in the three-prong modes to suppress fake π^0's introduced by the energy deposition of charged pions in the ECAL.
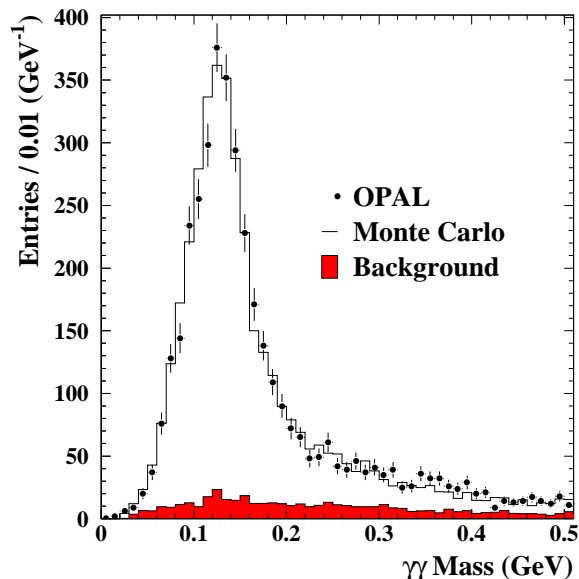

Figure 1: *The $\gamma\gamma$-mass in the $\pi\pi^0$ channel for decays with two reconstructed photons with a minimal energy of 0.5 GeV. OPAL data is shown as data points; the total Monte Carlo prediction is given by the open histogram and the shaded histogram denotes the τ and non-τ background.*

The granularity of the ECAL allows the reconstruction of both photons from a π^0 only if its energy is below $12\,\text{GeV}$. The π^0's with larger energies have photons which are merged in

the ECAL. Therefore all the photon candidates with energies above this value are considered to be π^0's and their momentum is calculated from the reconstructed energy corrected by the mass of the π^0.

5 Unfolding procedure

The Monte Carlo predictions for the measured spectra and their background contributions are corrected with the most recent constrained branching ratios of the τ given in [11]. Effects due to limited detector resolution and efficiency are accounted for by a regularized unfolding technique [45].

To unfold measured distributions in s (the squared mass of the hadronic final state) the detector simulation is used to create response matrices which map the generated distribution in $x \equiv s_{\mathrm{true}}$ to a $y \equiv s_{\mathrm{meas}}$ distribution one would measure including all detector effects. The following convolution integral describes the general relation between a true distribution $f(x)$ and a measured distribution $g(y)$:

$$g(y) = \int\limits_{x_{\min}}^{x_{\max}} \mathrm{d}x\, A(y,x)\, \epsilon(x)\, f(x) + b(y), \qquad (12)$$

where $A(y,x)$ is the detector response function, $b(y)$ denotes the background distribution, and $\epsilon(x)$ is the selection efficiency. Equation (12) can be simplified to a matrix equation of the form:

$$\mathbf{g} = \mathbf{A} \cdot \mathbf{f} + \mathbf{b}. \qquad (13)$$

This is performed in two steps. First, the true distribution $f(x)$ is parameterized with a set of m parameters f_j and m basis functions $p_j(x)$ which are defined below in equation (18):

$$f(x) = \sum_{j=1}^{m} f_j\, f_{\mathrm{MC}}(x)\, p_j(x), \qquad (14)$$

with $f_{\mathrm{MC}}(x)$ being the generated Monte Carlo distribution. By defining:

$$A_j(y) = \int\limits_{x_{\min}}^{x_{\max}} \mathrm{d}x\, \epsilon(x)\, f_{\mathrm{MC}}(x)\, A(y,x)\, p_j(x), \qquad (15)$$

equation (12) takes the form:

$$g(y) = \sum_{j=1}^{m} f_j\, A_j(y) + b(y). \qquad (16)$$

In the second step, $g(y)$, $b(y)$ and $A_j(y)$ are represented by n bins:

$$g_i = \int\limits_{y_{i-1}}^{y_i} \mathrm{d}y\, g(y); \qquad b_i = \int\limits_{y_{i-1}}^{y_i} \mathrm{d}y\, b(y); \qquad A_{ij} = \int\limits_{y_{i-1}}^{y_i} \mathrm{d}y\, A_j(y). \qquad (17)$$

The basis functions $p_j(x)$ used in equations (14) and (15) are chosen as cubic B-splines and thus have the following form:

$$p_j(x) = \frac{1}{6} \times \begin{cases} z^3 & z = (x - t_j\ \ )/d & t_j\ \ \le x < t_{j+1} \\ (1 + 3(1 + z(1 - z))z) & z = (x - t_{j+1})/d & t_{j+1} \le x < t_{j+2} \\ (1 + 3(1 + z(1 - z))(1 - z)) & z = (x - t_{j+2})/d & t_{j+2} \le x < t_{j+3} \\ (1 - z)^3 & z = (x - t_{j+3})/d & t_{j+3} \le x < t_{j+4} \\ 0 & & \text{otherwise} \end{cases} , \qquad (18)$$

where $d = (x_{\max} - x_{\min})/(m-3)$ is the distance between adjacent knots $t_k = x_{\min} + (k-4)\,d$ for $k = 1, \ldots, m-1$ knots and m splines.

The coefficient vector $\mathbf{f} = \{f_j\}$ is now observed in a fit to the data bins g_i, and the unfolded result can be obtained with equation (14). This particular choice of basis functions and normalization leads to the simple prediction $f_j = 1$ for all j if the Monte Carlo generated distribution and the unfolded result are identical.

In certain cases unfolding produces results with unphysical behavior. Statistically insignificant components of the fitted coefficient vector $\mathbf{f}$ can lead to large oscillations of the unfolded distribution. Therefore the unfolding needs to be modified by a regularization step which suppresses the statistically insignificant parts of the solution. This is achieved by applying a smooth damping function to the unfolded result. The magnitude of the fluctuations is measured by the total curvature $r(\mathbf{f})$ of the function $f(x)/f_{\mathrm{MC}}(x)$:

$$r(\mathbf{f}) = \int\limits_{x_{\min}}^{x_{\max}} \mathrm{d}x \left[\left(\frac{\mathrm{d}^2}{\mathrm{d}x^2} \frac{f(x)}{f_{\mathrm{MC}}(x)} \right) \right]^2 = \int\limits_{x_{\min}}^{x_{\max}} \mathrm{d}x \left[\sum_{j=1}^{m} f_j \frac{\mathrm{d}^2}{\mathrm{d}x^2} p_j(x) \right]^2 = \mathbf{f}^{\mathrm{T}} \cdot \mathbf{C} \cdot \mathbf{f}, \qquad (19)$$

where $\mathbf{C}$ is a constant, symmetric, positive semidefinite matrix obtained from the second derivatives of the basis functions p_j. The regularized result is now obtained by adding the total curvature $r(\mathbf{f})$ weighted with a regularization parameter ρ to the χ^2 in the fit and minimizing the sum:

$$\chi_{\mathrm{reg}}^2(\mathbf{f}) = \chi^2(\mathbf{f}) + \frac{1}{2}\,\rho\,r(\mathbf{f}). \qquad (20)$$

The final unfolded distribution in s is given by weighting the Monte Carlo distribution in s_{true} with the regularized coefficient vector $\mathbf{f}$ obtained from the fit (14).

This method is bias-free as long as the detector simulation is correct for all s and is independent of the used Monte Carlo distributions provided that only the statistically insignificant components of the fitted contributions are damped. Possible biases due to the detector simulation are accounted for in the systematic errors as described in section 7. The correct choice of the regularization parameter ρ can be tested in the following way:

a) The coefficients f_j, which are correlated and have in general different errors, can be transformed into a set of independent parameters a_j which have unit variance and are sorted with the regularization measure $\rho\,r(\mathbf{f})$ in order of decreasing significance [45]. All a_j with $j > n(\rho)$, where $n(\rho)$ is the number of effective coefficients remaining after damping with the parameter ρ, have to be consistent with zero.

b) Furthermore the χ^2-probability of the fit without the regularization term $r(\mathbf{f})$ should increase for the regularized coefficient vector $\mathbf{f}$.

The regularization parameter is chosen according to these criteria.

The background, in a particular one-prong (three-prong) channel, consists mainly of misidentified other one-prong (three-prong) τ decays, introducing correlations between the spectra. In order to provide a proper treatment of the correlations, the three one-prong (three-prong) channels are unfolded simultaneously. In addition to the three detector response matrices for the three one-prong (three-prong) signal modes, six more detector response matrices are used, mapping the Monte Carlo generated distribution in s_{true} of a background channel to the background part introduced by this channel in the s_{meas} distribution of a signal channel as correlated background. Non-τ background and other misidentified τ decays are treated as uncorrelated background b_i as described above.

6 Discussion of the measured spectra

The selection efficiencies and background fractions from simultaneously unfolded channels (correlated background) and other τ- and non-τ-background sources (uncorrelated background) are listed in table 1. Figures 2 and 3 show the measured s_{meas} distributions of the six channels

channel	efficiency	correlated background	uncorrelated background	selected decays
$\pi\pi^0$	$(28.7 \pm 0.1)\,\%$	$(7.7 \pm 0.2)\,\%$	$(7.9 \pm 0.1)\,\%$	32316
$\pi 2\pi^0$	$(18.8 \pm 0.1)\,\%$	$(45.0 \pm 0.6)\,\%$	$(8.4 \pm 0.1)\,\%$	13814
$\pi 3\pi^0$	$(8.0 \pm 0.2)\,\%$	$(70.0 \pm 2.2)\,\%$	$(11.4 \pm 0.5)\,\%$	1738
3π	$(34.6 \pm 0.1)\,\%$	$(9.7 \pm 0.3)\,\%$	$(3.8 \pm 0.1)\,\%$	14321
$3\pi\pi^0$	$(11.0 \pm 0.1)\,\%$	$(21.3 \pm 1.0)\,\%$	$(6.1 \pm 0.3)\,\%$	2455
$3\pi 2\pi^0$	$(8.3 \pm 0.4)\,\%$	$(82.3 \pm 2.9)\,\%$	$(7.1 \pm 0.5)\,\%$	1255

Table 1: *Efficiencies, background fractions and total number of selected τ decays.*

used in this analysis in comparison to the fitted signal after the regularized unfolding, and the Monte Carlo predictions.

The 3π spectrum shows a significant deviation from the shape predicted by the Monte Carlo (the dashed histogram) as has been observed in previous analyses of the 3π decay current [46]. There is also a slight deviation on the left side of the peak in the $\pi\pi^0$ channel and in the upper tail region. The other modes are statistically consistent with their Monte Carlo predictions.

The χ^2 values for the one-prong and three-prong fits after the regularization step are $\chi^2_{1-\mathrm{pr.}}/\mathrm{d.o.f.} = 94.0/109$ and $\chi^2_{3-\mathrm{pr.}}/\mathrm{d.o.f} = 71.4/69$ leading to the χ^2-probabilities 0.85 and 0.40, respectively.

The unfolded distributions of the measured spectra are shown in figure 4. The plotted data points are strongly correlated due to the unfolding procedure. The deviations from the Monte Carlo prediction seen in figures 2 and 3 are still present after the unfolding, most prominently in the $\pi\pi^0$ and the 3π channel. The enhancement in the upper tail (see figures 2 (b) and 4 (a)) of the $\pi\pi^0$ distribution can be explained within the Kühn–Santamaria model [47] by enlarging the fraction of $\rho(1450)$'s and $\rho(1700)$'s in the ρ decay amplitude. A similar correction to the three-pion current, modelled as a Breit–Wigner decay chain $\mathrm{a}_1 \to \rho\pi \to 3\pi$ [47] in the Monte Carlo, does not account for the observed discrepancy.

7 Systematic uncertainties

Possible origins for systematic effects on the reconstructed value for the squared hadronic mass, s_{meas}, come from the uncertainty in the energy scale for reconstructed photons and the uncertainty in the momentum scale for tracks, while the wrong choice of the regularization parameter ρ in the unfolding can distort the unfolded distributions.

The energy resolution can be tested by measuring the invariant mass of the two photons from π^0 decays. A systematic shift in the observed mass in the data compared to the detector simulation can be translated into a scale factor for the reconstructed photon energies. Deviations of $(0.5 \pm 0.9)\,\mathrm{MeV}$ for m_{π^0} have been observed between data and Monte Carlo (figure 1). This corresponds to an energy scale factor of 1.004 ± 0.007. The energies of the reconstructed
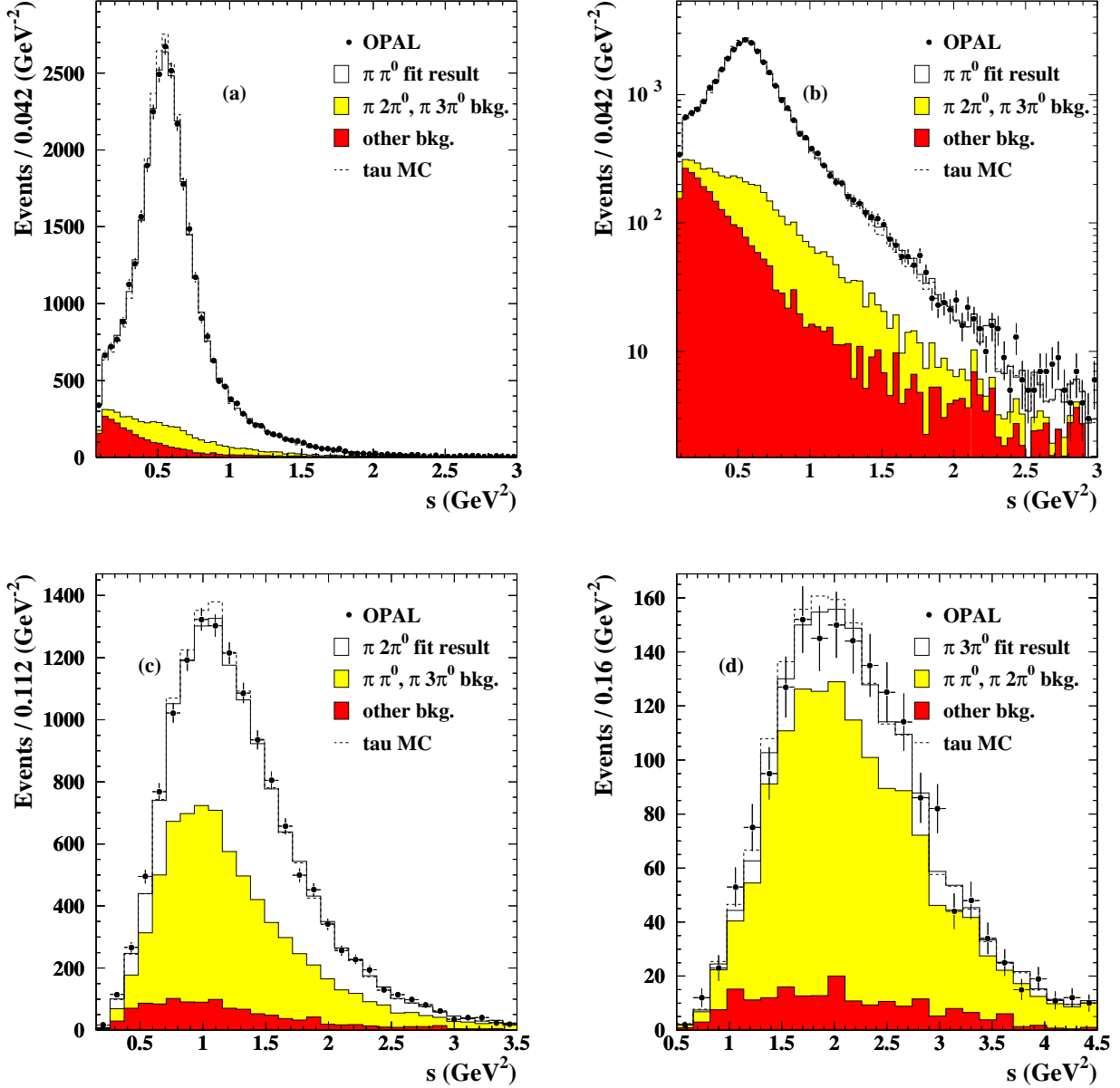
Figure 2: *The measured s_{meas} spectra for 1-prong decays. Plots (a) and (b) are the $\pi\pi^0$ channel, (c) and (d) are the $\pi 2\pi^0$ and $\pi 3\pi^0$ modes, respectively. The points denote OPAL data (statistical errors only). The open histograms show the fitted spectra after the regularized unfolding, refolded into detector space. The background contributions from simultaneously unfolded channels (correlated background) are shown as light grey areas while the background from other sources (uncorrelated background) is represented in dark grey.*
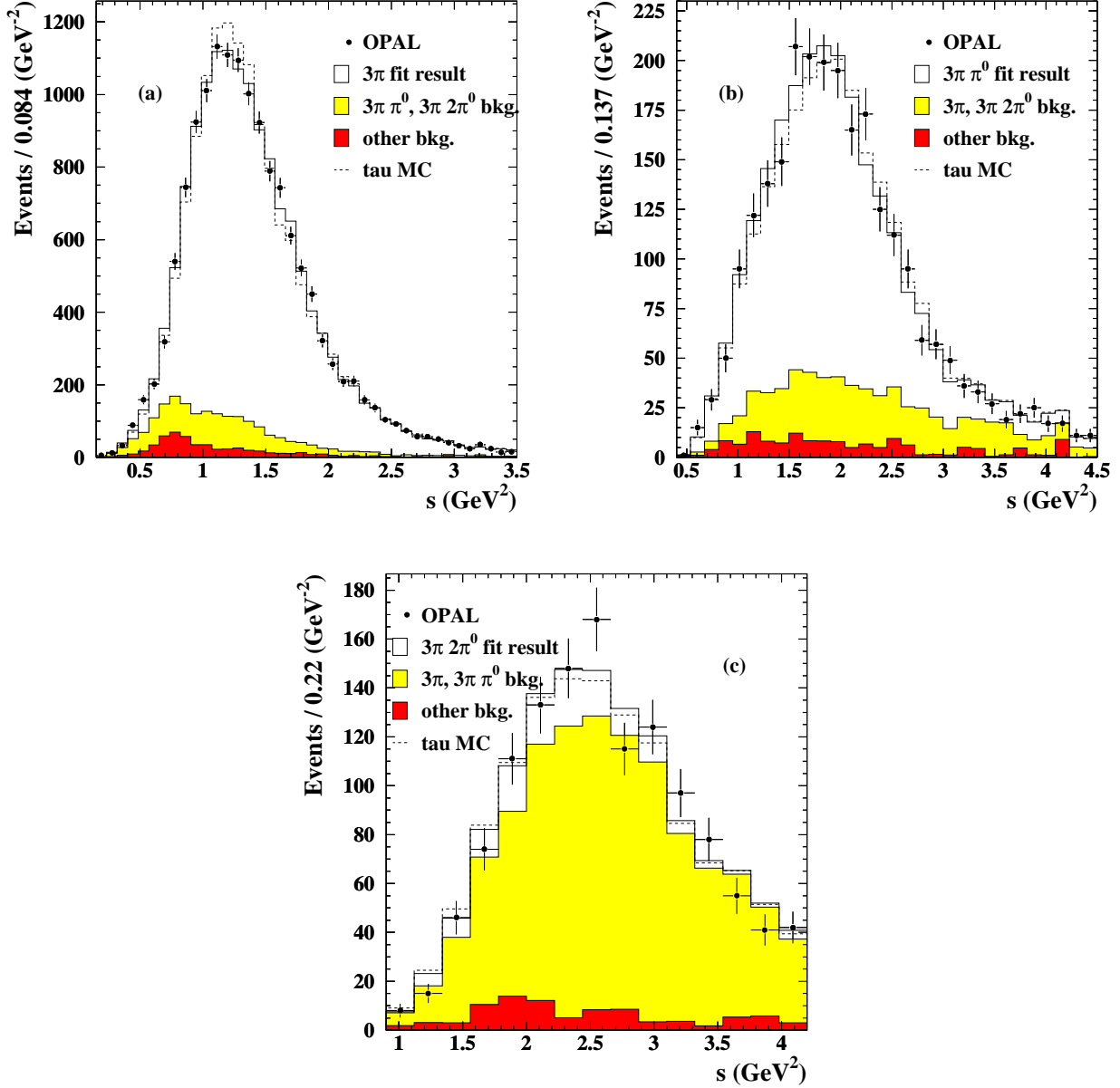
Figure 3: *The measured s_{meas} spectra for 3-prong decays. Plot (a) is the 3π channel, (b) and (c) are the $3\pi\pi^0$ and $3\pi2\pi^0$ modes, respectively. The points denote OPAL data (statistical errors only). The open histograms show the fitted spectra after the regularized unfolding, refolded into detector space. The background contributions from simultaneously unfolded channels (correlated background) are shown as light grey areas while the background from other sources (uncorrelated background) is represented in dark grey.*
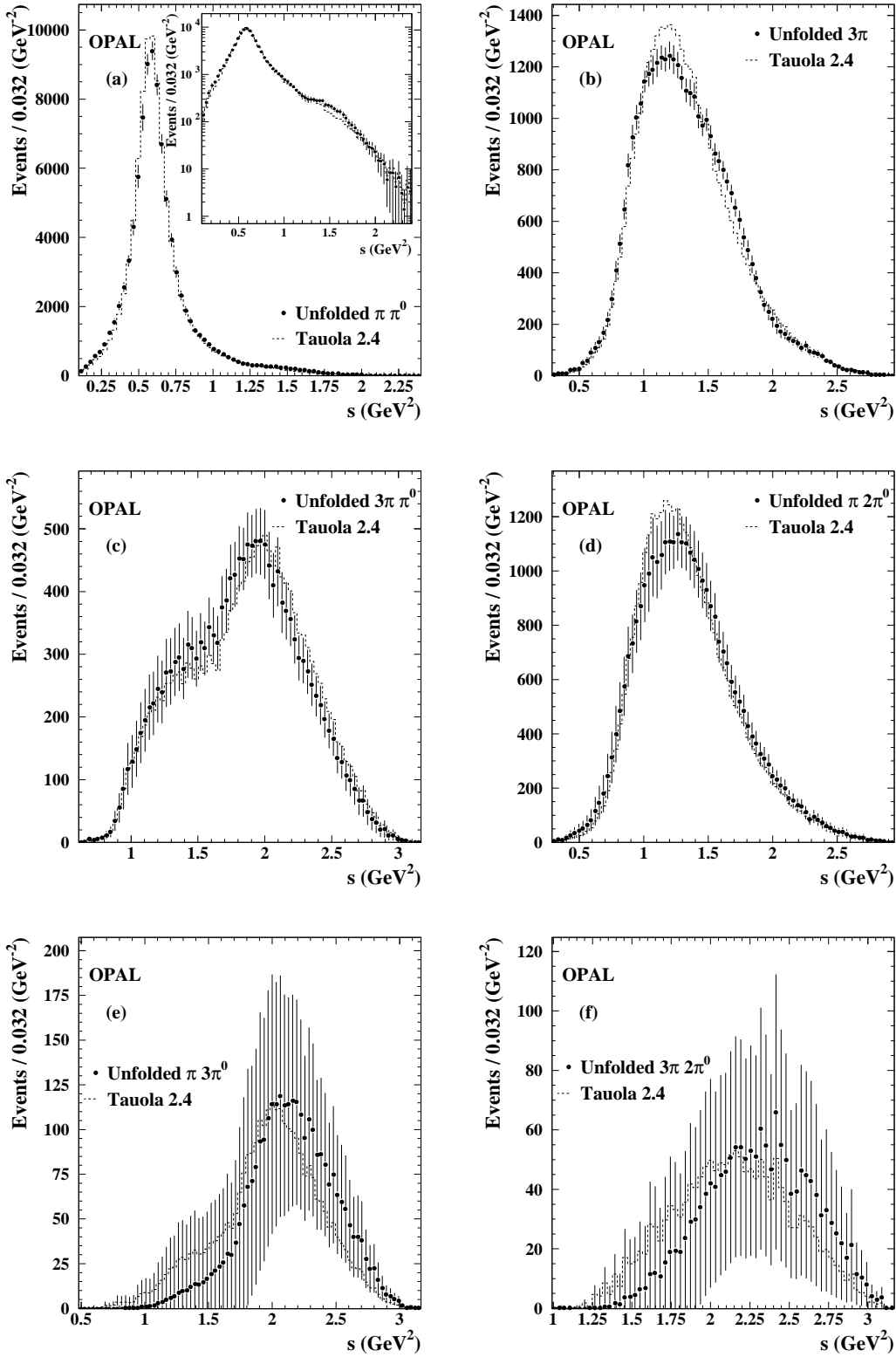
Figure 4: *The unfolded s_{true} spectra. Shown are the three vector channels (left) and the three axial-vector channels (right) together with the Monte Carlo prediction. There are strong correlations between the data points due to the unfolding. The plots (a),(d),(e) are the unfolded spectra of plots (a),(c),(d) in figure 2 and the plots (b),(c),(f) are the unfolded spectra of the plots (a),(b),(c) in figure 3. The error bars include statistical and systematic uncertainties.*

photons in the Monte Carlo samples are varied by $\pm 0.7\,\%$ in order to estimate the systematic error due to this effect[5].

The uncertainty in the momentum of the tracks have been studied using μ pairs. The Monte Carlo is corrected for observed deviations between data and Monte Carlo in the mean and the width of the momentum distribution. The momenta and the momentum resolution of all tracks in the Monte Carlo samples are scaled due to the uncertainties in these corrections, thus leading to the quoted systematic errors.

The damping parameter ρ in the regularization step of the unfolding procedure is calculated from the number of effectively remaining spline coefficients after the regularization. This number is chosen so that the test conditions a) and b) given in section 5 are satisfied. The default value (16 effective splines from 48 total splines for the 1-prong fit and 16 effective splines from 36 total splines for the 3-prong fit) is varied by ± 4 for both fits, where the range is derived from Monte Carlo tests of the unfolding procedure: the tests consist of unfolding fake data samples in the $\rho \to \pi\pi^0$ channel. The mass and the width of the ρ in the fake data samples at the generator level are different from the values used in the standard Monte Carlo which is used to create the response matrix. The allowed range of the damping parameter is then determined by comparing the unfolded fake data samples with their generator level distributions for different choices of the damping parameter, for which the test conditions a) and b) are satisfied. Within this range the unfolded distributions reproduce the mass spectrum of the modified ρ without biases towards the generator distribution of the standard Monte Carlo. The uncertainty due to the variation of the damping parameter is added as a systematic error on the unfolded results.

Uncertainties of statistical nature from the errors on the branching ratios (see table 2), the limited statistics of signal and background Monte Carlo samples, and on the efficiencies are incorporated in the unfolding procedure by adding them in quadrature to the statistical errors on the data.

Systematic effects related to photon and π^0 detection efficiency are largely covered by the systematic errors.

8 Results

8.1 Moments of R_τ

The unfolded spectra of the hadronic modes shown in figure 4 are normalized to their branching fractions and summed up to the vector and axial-vector spectra with their appropriate weights:

$$R^{kl}_{\tau,\mathrm{V/A}}(s_0) = \int\limits_0^{s_0} \mathrm{d}s \left(1 - \frac{s}{s_0}\right)^k \left(\frac{s}{m_\tau^2}\right)^l \sum_{\mathrm{h_{V/A}}} \frac{B(\tau \to \mathrm{h_{V/A}}\nu_\tau)}{B(\tau \to \mathrm{e}\nu_\mathrm{e}\nu_\tau)} \frac{w_{\mathrm{V/A}}}{N_{\mathrm{V/A}}} \frac{\mathrm{d}N_{\mathrm{V/A}}}{\mathrm{d}s}, \tag{21}$$

where $N_{\mathrm{V/A}}$ is the number of taus that decay into the hadron $\mathrm{h_{V/A}}$ plus neutrino, and $w_{\mathrm{V/A}}$ denotes the appropriate weight of the hadronic mode to the vector or axial-vector current. The branching ratios of the hadronic modes (and the lepton channels), together with their contributing weights for the vector and axial-vector spectra, are summarized in table 2.

The hadronic modes $\omega\pi$, $\omega\pi\pi^0$ and $\eta\pi\pi^0$ involve decays of ω's and η's, and do not conserve isospin symmetry, since their decay can occur via the electromagnetic interaction. Therefore, the unfolded distributions in the 3π mode, which is considered to belong to the axial-vector

---

[5]Since the invariant two-photon mass depends also on the angle between the two photons, this energy scale factor accounts for systematic uncertainties in the energy resolution and the angular resolution of the ECAL.

$\tau \to \nu_\tau X$	$B[\%]$	w_V	w_A	comment
$e\nu_e$	17.83 ± 0.08	–	–	
$\mu\nu_\mu$	17.35 ± 0.10	–	–	
$\pi\pi^0$	25.24 ± 0.16	1.0	0.0	
$3\pi\pi^0$	4.26 ± 0.09	1.0	0.0	including $\omega\pi$ and $\omega\pi\pi^0$
$\pi 3\pi^0$	1.14 ± 0.14	1.0	0.0	
π	11.31 ± 0.15	0.0	1.0	
3π	9.26 ± 0.12	0.0	1.0	$3h - 2K\pi - K2\pi$ including $\omega\pi$
$\pi 2\pi^0$	9.27 ± 0.14	0.0	1.0	
$3\pi 2\pi^0$	0.50 ± 0.05	0.0	1.0	including $\omega\pi\pi^0$ and $\eta\pi\pi^0$
5π	0.075 ± 0.007	0.0	1.0	MC
$\pi 4\pi^0$	0.12 ± 0.06	0.0	1.0	MC
$3\pi 3\pi^0$	0.11 ± 0.06	1.0	0.0	MC
$5\pi\pi^0$	0.022 ± 0.005	1.0	0.0	MC
KK^0	0.16 ± 0.03	1.0	0.0	MC
$2K\pi$	0.10 ± 0.03	0.5 ± 0.5	0.5 ± 0.5	MC
$2K^0\pi$	0.10 ± 0.02	0.5 ± 0.5	0.5 ± 0.5	MC
$KK^0\pi^0$	0.14 ± 0.03	0.5 ± 0.5	0.5 ± 0.5	MC
$\omega\pi$	0.21 ± 0.01	1.0	-0.2	MC excluding $3\pi\pi^0$
$\omega\pi\pi^0$	0.046 ± 0.007	-0.25	1.0	excluding $3\pi 2\pi^0$
$\eta\pi\pi^0$	0.17 ± 0.03	1.0	-0.24	MC
$X_{strange}$	2.67 ± 0.14	–	–	

Table 2: *Branching ratios for the hadron modes and lepton channels. Shown are the fitted values from the Particle Data Group [11] and the contributing weights for the vector and axial-vector current. Channels marked with MC are 'generator-level' Monte Carlo channels included in the spectra. Negative weights are used to subtract inclusively measured contributions from the wrong current.*

current, and in the $3\pi\pi^0$ mode, which belongs to the vector current, are contaminated by decays not belonging to the assigned currents (e.g. $\omega\pi \to 3\pi$), and thus need to be corrected. Since $\sim 71\%$ of the $3\pi 2\pi^0$ mode consist of $\omega\pi\pi^0$ decays, this channel is used for the $\omega\pi\pi^0$ corrections. Corrections for the other ω and η modes are made with the Monte Carlo. Decay modes which are not reconstructed from the data have also to be included in the total vector and axial-vector spectra. Their distributions are taken from the Monte Carlo. The $2K\pi$ modes contribute to both classes to an unknown amount. A weight of $(50 \pm 50)\%$ is used for both currents and a correlation of -100% between the vector and the axial-vector weights is assumed. The errors assigned to Monte Carlo spectra are taken to be $\pm 100\%$, in order to take a possible mismodelling of the Monte Carlo into account.

The moments $R_{V/A}^{kl}$ are given in table 3. The errors on the moments are subdivided into statistical uncertainties due to the data statistics, the uncertainties comming from the branching ratio errors, and systematic uncertainties induced by the limited Monte Carlo statistics and the variations of the energy scale, the momentum scale, and the regularization parameter (table 4). Correlations between the moments are given in table 5.

moment kl	R_V^{kl}	total error	R_A^{kl}	total error
00	1.764	± 0.016	1.720	± 0.017
10	1.264	± 0.012	1.240	± 0.013
11	0.2980	± 0.0034	0.2510	± 0.0032
12	0.0942	± 0.0019	0.1090	± 0.0019
13	0.0403	± 0.0016	0.0518	± 0.0013

Table 3: *The measured moments $R_{V/A}^{kl}$, for $kl = 00, 10, 11, 12, 13$. The errors shown represent statistical and systematic uncertainties.*

	kl	data stat.	branching ratios	systematic errors			
				MC stat.	E scale	p scale	regularization
	00	–	± 0.016	–	–	–	–
	10	± 0.005	± 0.010	± 0.004	± 0.004	± 0.001	± 0.001
V	11	± 0.0012	± 0.0031	± 0.0008	± 0.0005	± 0.0002	± 0.0000
	12	± 0.0006	± 0.0016	± 0.0004	± 0.0007	± 0.0000	± 0.0001
	13	± 0.0008	± 0.0011	± 0.0005	± 0.0005	± 0.0001	± 0.0001
	00	–	± 0.017	–	–	–	–
	10	± 0.004	± 0.012	± 0.002	± 0.002	± 0.002	± 0.003
A	11	± 0.0010	± 0.0029	± 0.0007	± 0.0003	± 0.0002	± 0.0004
	12	± 0.0008	± 0.0015	± 0.0005	± 0.0006	± 0.0001	± 0.0005
	13	± 0.0007	± 0.0008	± 0.0004	± 0.0004	± 0.0002	± 0.0003

Table 4: *Statistical and systematic uncertainties of the measured moments. The upper (lower) portion of the table contains the result for the vector (axial-vector) current.*

8.2 Spectral functions

The vector and axial-vector spectral functions are given by inverting equation (1):

$$
\begin{aligned}
v/a(s) &= 2\pi \,\mathrm{Im}\Pi_{V/A}^{(1)}(s) \\
&= m_\tau^2 \left[6 S_{\mathrm{EW}} |V_{\mathrm{ud}}|^2 \left(1 - \frac{s}{m_\tau^2}\right)^2 \left(1 + 2\frac{s}{m_\tau^2}\right) \right]^{-1} \\
&\quad \times \sum_{\mathrm{h_{V/A}}} \frac{B(\tau \to \mathrm{h_{V/A}}\nu_\tau)}{B(\tau \to \mathrm{e}\nu_{\mathrm{e}}\nu_\tau)} \frac{w_{\mathrm{V/A}}}{N_{\mathrm{V/A}}} \frac{\mathrm{d}N_{\mathrm{V/A}}}{\mathrm{d}s},
\end{aligned}
\tag{22}
$$

where the sum is performed over hadronic final states $h_{V/A}$ with angular momentum $J = 1$.

The spectral functions (and their correlations) are shown in figure 5 together with the flat naïve parton model prediction $v_{\mathrm{naïve}}(s) = a_{\mathrm{naïve}}(s) = 1/2$ and the prediction of perturbative QCD (massless) for $\alpha_{\mathrm{s}}(m_{\mathrm{Z}}^2) = 0.122$ which increases the naïve prediction by $\approx 10\,\%$. As a result of the regularized unfolding, the bin-to-bin correlations are of the order of $+80\,\%$ $(-50\,\%)$ for bin distances of $0.1\,\mathrm{GeV}^2$ ($\approx 1\,\mathrm{GeV}^2$). The correlation between vector and axial-vector spectral function varies from $-60\,\%$ to $+60\,\%$. Figure 6 shows the difference and the sum of the two measured spectral functions. The function $v(s) - a(s)$ should vanish in the limit of perturbative, massless QCD. The deviation from this prediction, e.g. due to the ρ and a_1 resonances, indicates the large sensitivity of this distribution to non-perturbative effects. The QCD prediction for
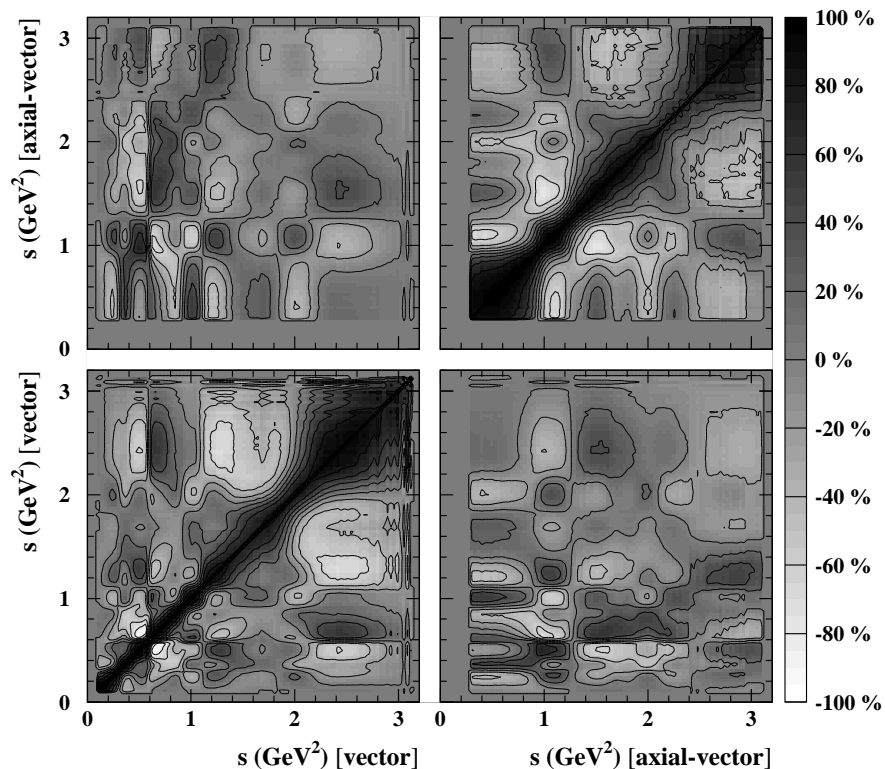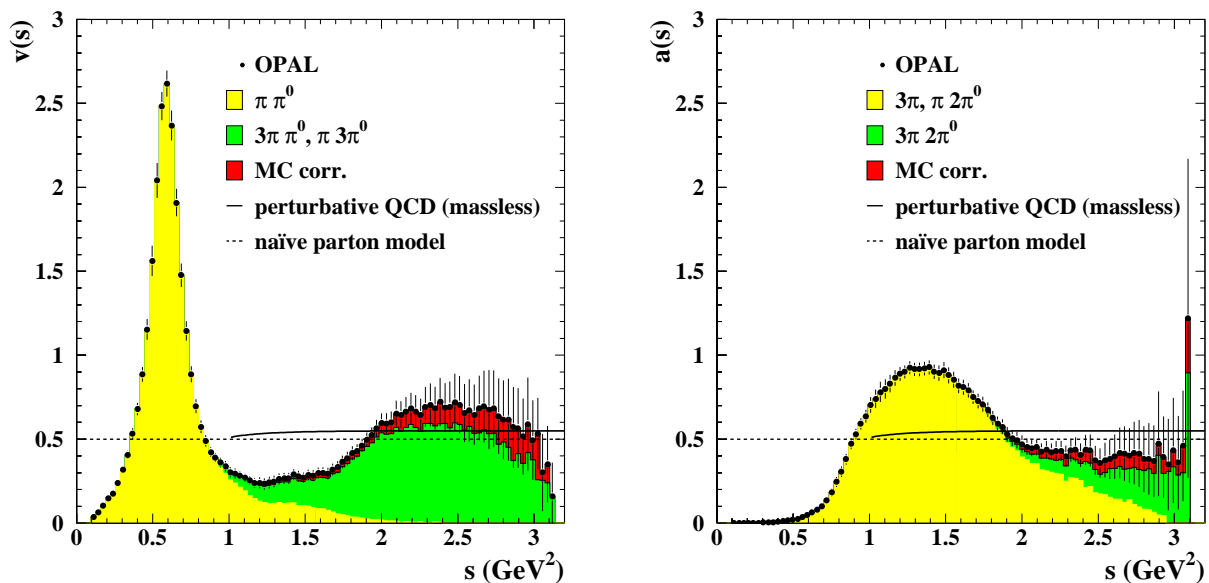
Figure 5: *The vector and axial-vector spectral functions. Shown are the sums of all contributing channels as data points (upper two plots). Some exclusive contributions are shown as shaded areas. The naïve parton model prediction is shown as dashed line, while the solid line depicts the perturbative, massless QCD prediction for $\alpha_s(m_Z^2) = 0.122$. The error bars include statistical and systematic uncertainties. The pion pole is subtracted from the axial-vector spectrum. The lower plot shows the correlations of the two spectral functions in continuous gray-levels from white to black which correspond to the correlations in percent from $-100\,\%$ to $+100\,\%$. The contour lines are drawn in equidistant steps of $20\,\%$.*

20

V	00	10	11	12
10	72			
11	87	72		
12	74	14	72	
13	53	−18	37	90

A\V	00	10	11	12	13
00	2	9	0	−8	−8
10	9	4	0	4	8
11	−5	−2	−7	−7	−4
12	−8	3	0	−12	−17
13	−10	8	3	−16	−26

A	00	10	11	12
10	85			
11	79	56		
12	64	22	85	
13	51	2	63	94

Table 5: *Correlations between the measured moments $R^{kl}_{V/A}$ in percent. The left (right) table gives the correlations between the moments of the vector (axial-vetor) current; the table in the middle shows the correlations between the moments of different currents.*

$v(s) + a(s)$ which is $\approx 10\,\%$ above the naïve expectation $v(s) + a(s) = 1$ as in figure 5 gives a reasonable description of the region $s > 1\,\mathrm{GeV}^2$. The structure due to the narrow resonances in the region below $s \simeq 1\,\mathrm{GeV}^2$ is however not described by perturbative QCD.
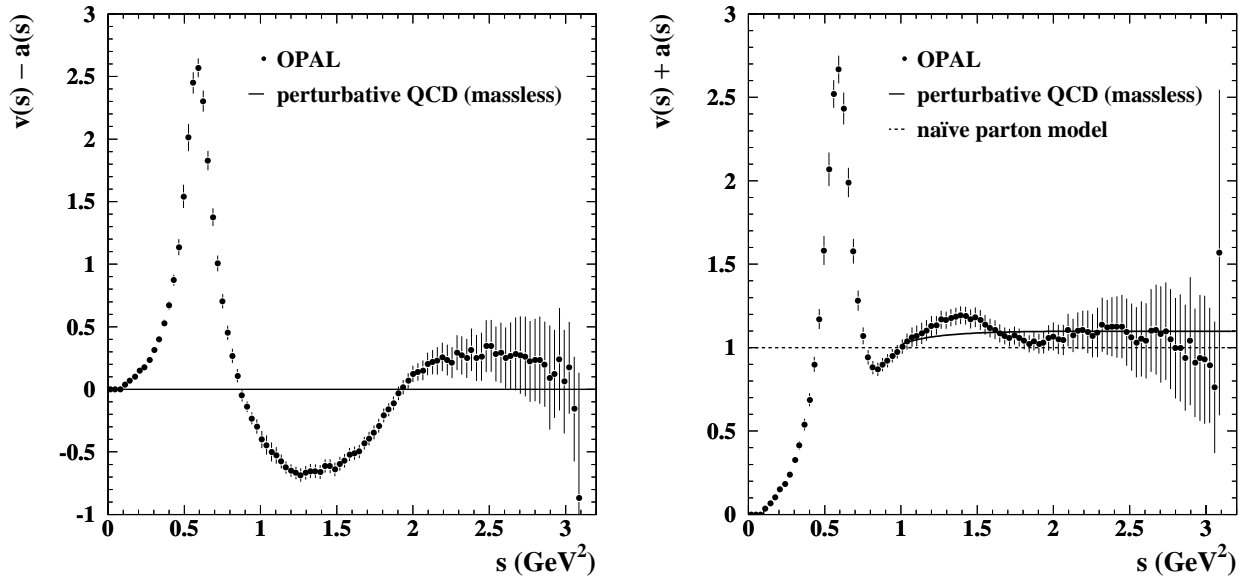

Figure 6: *The difference (sum) of the spectral functions $v(s) - a(s)$ $(v(s) + a(s))$. The dashed line is the naïve parton model expectation and the solid lines depict the prediction of massless, perturbative QCD as in figure 5. For $v(s) - a(s)$ both predictions are identically zero.*

9 Measurement of the strong coupling α_{s}

Since the perturbative expansions for vector and axial-vector currents are identical while the non-perturbative parts have opposite sign but the same order of magnitude for both currents, two different fits are used for the extraction of α_{s} and the power corrections, respectively. The sum of vector and axial-vector moments is most sensitive to perturbative QCD and is used for the measurement of α_{s} (fit 1) while the separate moments of both currents are used to obtain the power corrections (fit 2). In addition to the moments listed in table 3 it is possible to include the measurements of the τ lifetime τ_τ and the branching ratio $B_\mu = B(\tau \to \mu\nu_\mu\nu_\tau)$ in

fit 1 since each of them can be used to predict the total hadronic decay rate of the τ lepton:

$$R_\tau(\tau_\tau) \ = \ \frac{1}{\Gamma_{\mathrm{e}}}\frac{1}{\tau_\tau} - 1 - \frac{\Gamma_\mu}{\Gamma_{\mathrm{e}}}, \tag{23}$$

$$R_\tau(B_\mu) \ = \ \frac{\Gamma_\mu}{\Gamma_{\mathrm{e}}}\frac{1}{B_\mu} - 1 - \frac{\Gamma_\mu}{\Gamma_{\mathrm{e}}}. \tag{24}$$

Both equations assume lepton universality so that the following equation holds:

$$B_\mu = B_{\mathrm{e}}\frac{\Gamma_\mu}{\Gamma_{\mathrm{e}}}, \tag{25}$$

with $\frac{\Gamma_\mu}{\Gamma_{\mathrm{e}}} = 0.9726$ [10] and $\Gamma_{\mathrm{e}} = 4.0329 \cdot 10^{-13}$ GeV [10, 48]. The non-strange decay rate of the τ lepton is then obtained by subtracting $R_{\tau,\mathrm{s}} = B_{\mathrm{s}}/B_{\mathrm{e}} = 0.150 \pm 0.008$ [11] from the weighted average $R_\tau(B_\mu, \tau_\tau)$ of $R_\tau(\tau_\tau)$ and $R_\tau(B_\mu)^6$. In principle the electron branching ratio B_{e} could also be used to determine R_τ but this has a 96 % correlation with R_τ from the hadronic modes due to the correlations of the constrained branching ratios in [11].

Using the world average $\tau_\tau = (291.0 \pm 1.5)$ fs and the fitted value $B_\mu = 0.1735 \pm 0.0010$ [11] one gets:
$$R_\tau(B_\mu, \tau_\tau) - R_{\tau,\mathrm{s}} = 3.485 \pm 0.023. \tag{26}$$
From the vector and axial-vector decay rates in table 3 one gets the following value:

$$R_{\tau,\mathrm{V}} + R_{\tau,\mathrm{A}} = 3.484 \pm 0.024. \tag{27}$$

In the first fit, four parameters are used to describe the five moments, leaving one degree of freedom for the fit: the strong coupling $\alpha_{\mathrm{s}}(m_\tau^2)$, the gluon condensate $\langle \frac{\alpha_{\mathrm{s}}}{\pi} GG \rangle$ and the dimension 6 and 8 contributions to the $kl = 00$ moments $\delta_{\mathrm{V+A}}^6$, $\delta_{\mathrm{V+A}}^8$. The second fit requires six parameters to predict ten moments (four degrees of freedom): $\alpha_{\mathrm{s}}(m_\tau^2)$, $\langle \frac{\alpha_{\mathrm{s}}}{\pi} GG \rangle$ and the power corrections δ_{V}^6, δ_{V}^8, δ_{A}^6 and δ_{A}^8. The power corrections from the two fits can be compared via the following relation:
$$\delta_{\mathrm{V+A}}^D = \frac{1}{2}\left(\delta_{\mathrm{V}}^D + \delta_{\mathrm{A}}^D\right). \tag{28}$$
Further inputs for both fits are the quark masses for the three light quarks $m_{\mathrm{u,d,s}}$

$$m_{\mathrm{u}} = (8.7 \pm 1.5)\,\mathrm{MeV}, \quad m_{\mathrm{d}} = (15.4 \pm 1.5)\,\mathrm{MeV}, \quad m_{\mathrm{s}} = (270 \pm 30)\,\mathrm{MeV}, \tag{29}$$

and the quark condensates $\langle \overline{\psi}\psi \rangle_{\mathrm{u,d,s}} = -\mu_{\mathrm{u,d,s}}^3$, with

$$\mu_{\mathrm{u}} = \mu_{\mathrm{d}} = (189 \pm 7)\,\mathrm{MeV}, \quad \mu_{\mathrm{s}} = (160 \pm 10)\,\mathrm{MeV}. \tag{30}$$

The values are taken from [4]. The error matrix of the moments is calculated from the experimental errors on the moments and their correlations (tables 3 and 5) and the theoretical error matrix calculated from the errors on the quark-masses and quark-condensates. The results from the fit to the sum of vector and axial-vector moments is given in table 6. The quoted errors are subdivided into a statistical error due to the data statistics, the uncertainty induced by the errors on the branching ratios, an experimental systematic error from the Monte Carlo statistics and the unfolding procedure, and a theoretical error including the uncertainties on quark masses, the variation of the $O(\alpha_{\mathrm{s}}^4)$ coefficient, the renormalization scheme dependence, and the renormalization scale uncertainty. The strong coupling is most sensitive to the $kl = 00$

| theory | observable | value | contributing errors | | | | χ^2/d.o.f. |
			data	B	syst.	theo.	
CIPT	$\alpha_s(m_\tau^2)$	0.348	± 0.002	± 0.009	± 0.002	± 0.019	
	$\langle \frac{\alpha_s}{\pi} GG \rangle / \mathrm{GeV}^4$	-0.003	± 0.007	± 0.007	± 0.006	± 0.005	0.16/1
	$\delta_{\mathrm{V+A}}^6$	0.0012	± 0.0034	± 0.0033	± 0.0029	± 0.0006	
	$\delta_{\mathrm{V+A}}^8$	-0.0010	± 0.0024	± 0.0016	± 0.0015	± 0.0003	
FOPT	$\alpha_s(m_\tau^2)$	0.324	± 0.001	± 0.006	± 0.002	± 0.013	
	$\langle \frac{\alpha_s}{\pi} GG \rangle / \mathrm{GeV}^4$	0.014	± 0.007	± 0.006	± 0.005	± 0.013	0.17/1
	$\delta_{\mathrm{V+A}}^6$	0.0028	± 0.0034	± 0.0034	± 0.0030	± 0.0068	
	$\delta_{\mathrm{V+A}}^8$	-0.0015	± 0.0024	± 0.0016	± 0.0014	± 0.0019	
RCPT	$\alpha_s(m_\tau^2)$	0.306	± 0.001	± 0.005	± 0.001	± 0.011	
	$\langle \frac{\alpha_s}{\pi} GG \rangle / \mathrm{GeV}^4$	-0.002	± 0.007	± 0.007	± 0.005	± 0.002	0.07/1
	$\delta_{\mathrm{V+A}}^6$	-0.0047	± 0.0036	± 0.0040	± 0.0032	± 0.0011	
	$\delta_{\mathrm{V+A}}^8$	-0.0001	± 0.0024	± 0.0017	± 0.0015	± 0.0003	

Table 6: *The result for $\alpha_s(m_\tau^2)$ and the non-perturbative parameters from the fit to the sum of vector and axial-vector moments. Shown are the values for the three different descriptions of the perturbative part of the moments (see text). The given errors correspond to the data statistics, the uncertainty due to the errors on the branching ratios B, a systematic error from the Monte Carlo statistics, the energy scale, the momentum scale, and the unfolding, and a total theoretical uncertainty.*

moment, and therefore the dominant contribution to the experimental uncertainty on α_s comes from the uncertainties on the branching ratios.

All three theories lead to similar χ^2 values (see table 6) but the spread in the fitted values for $\alpha_s(m_\tau^2)$ exceeds the total uncertainties by a factor of two. A similar spread of the values for $\alpha_s(m_\tau^2)$ from the three models has also been observed in [8, 49], where RCPT has led to the lowest value and CIPT to the largest value in agreement with our results (table 6).

The differences in the statistical and systematic errors on α_s are induced by the scaling of the relative error with α_s and thus are compatible for the three fits. The theoretical uncertainties should also obey this scaling behavior: here the fits for FOPT and CIPT only include the uncertainty on the unknown K_4 coefficient and hence cannot be compared to the RCPT result. Furthermore the uncertainty due to the variation of the renormalization scheme vanishes for RCPT. The impact on α_s from the various theoretical error sources is listed in table 7. The given errors correspond to the spread of the fitted values of α_s in fit 1 due to the unknown $O\left(\alpha_s^4\right)$ dependence $K_4 = 25 \pm 50$, the choice of renormalization scale $0.4 \leq \mu^2/m_\tau^2 \leq 2.0$, the variation of the renormalization scheme parameterized with the third coefficient of the β-function $0.0 \leq \beta_3^{\mathrm{RS}}/\beta_3^{\overline{\mathrm{MS}}} \leq 2.0$, and the evolution of $\alpha_s(m_\tau^2)$ to the Z^0-mass scale.

Although the total theoretical uncertainties on α_s are compatible for all three theories there is a major difference between FOPT and the two other models: the FOPT fit leads to

---

[6]$R_{\tau,\mathrm{s}}$ is subtracted from R_τ, since the induced dependency on the mass of the strange quark would lead to a larger uncertainty in the fits if R_τ would be used instead.

error source	$\Delta\alpha_{\mathrm{s}}(m_\tau^2)$			$\Delta\alpha_{\mathrm{s}}(m_{\mathrm{Z}}^2)$		
	CIPT	FOPT	RCPT	CIPT	FOPT	RCPT
$-25 \leq K_4 \leq 75$	±0.012	±0.006	–	±0.0013	±0.0007	–
$0.4 \leq \mu^2/m_\tau^2 \leq 2.0$	±0.006	±0.009	±0.011	±0.0005	±0.0009	±0.0015
$0.0 \leq \beta_3^{\mathrm{RS}}/\beta_3^{\overline{\mathrm{MS}}} \leq 2.0$	±0.015	±0.009	±0.000	±0.0009	±0.0005	±0.0005
evolution	–	–	–	±0.0003	±0.0003	±0.0003

Table 7: *The theoretical uncertainties on the strong coupling constant. The errors correspond to the full spread of the fitted α_s values in fit 1 due to the variation of the parameters listed in the first column.*

a significant larger dependency of the non-perturbative parameters $\langle\frac{\alpha_{\mathrm{s}}}{\pi}GG\rangle$ and $\delta_{\mathrm{V+A}}^{6/8}$ on the theoretical uncertainties than CIPT and RCPT. The dominant effect comes from the variation of the renormalization scale μ^2. The statistical and systematic uncertainties on the power corrections are very similar for all three theories, agreeing with expectation. Figure 7 shows a comparison of $R_{\tau,\mathrm{V}}(s_0) + R_{\tau,\mathrm{A}}(s_0)$ as predicted from the three theories using the fit results at $s_0 = m_\tau^2$ with the data. The Contour Improved prediction is consistent with the data from the τ-mass scale down to $s_0 \approx 1\,\mathrm{GeV}^2$ while FOPT and RCPT tend to predict too large values below $s_0 \approx 2\,\mathrm{GeV}^2$.

9.1   Evolution of α_{s} from m_τ to m_{Z}

The value of the strong coupling at the mass scale of the τ lepton can be evolved up to the mass scale of the Z^0. This is done by solving the four-loop β-function given by equation (7) numerically in small steps from m_τ^2 to m_{Z}^2 applying a three-loop matching condition [50] at the flavor thresholds for $m_{\mathrm{c}}(m_{\mathrm{c}}) = (1.30 \pm 0.06)\,\mathrm{GeV}$ and $m_{\mathrm{b}}(m_{\mathrm{b}}) = (4.13 \pm 0.06)\,\mathrm{GeV}$ [50]. The evolution procedure induces an additional error of ±0.0003 [50] on the strong coupling at the Z^0 mass. Using the CIPT result for $\alpha_{\mathrm{s}}(m_\tau^2)$ and $m_{\mathrm{Z}} = 91.187\,\mathrm{GeV}$ the following value is obtained:

$$\alpha_{\mathrm{s}}(m_{\mathrm{Z}}^2) = 0.1219 \pm 0.0010_{\mathrm{exp}} \pm 0.0017_{\mathrm{theo}} \pm 0.0003_{\mathrm{evol}}. \tag{31}$$

The FOPT fit gives

$$\alpha_{\mathrm{s}}(m_{\mathrm{Z}}^2) = 0.1191 \pm 0.0008_{\mathrm{exp}} \pm 0.0013_{\mathrm{theo}} \pm 0.0003_{\mathrm{evol}}. \tag{32}$$

Finally RCPT gives:

$$\alpha_{\mathrm{s}}(m_{\mathrm{Z}}^2) = 0.1169 \pm 0.0007_{\mathrm{exp}} \pm 0.0015_{\mathrm{theo}} \pm 0.0003_{\mathrm{evol}}. \tag{33}$$

The different contributions to the theoretical uncertainties are listed in table 7. The results are in good agreement with the value obtained from fits to combined electroweak measurements at LEP and SLD [51]:

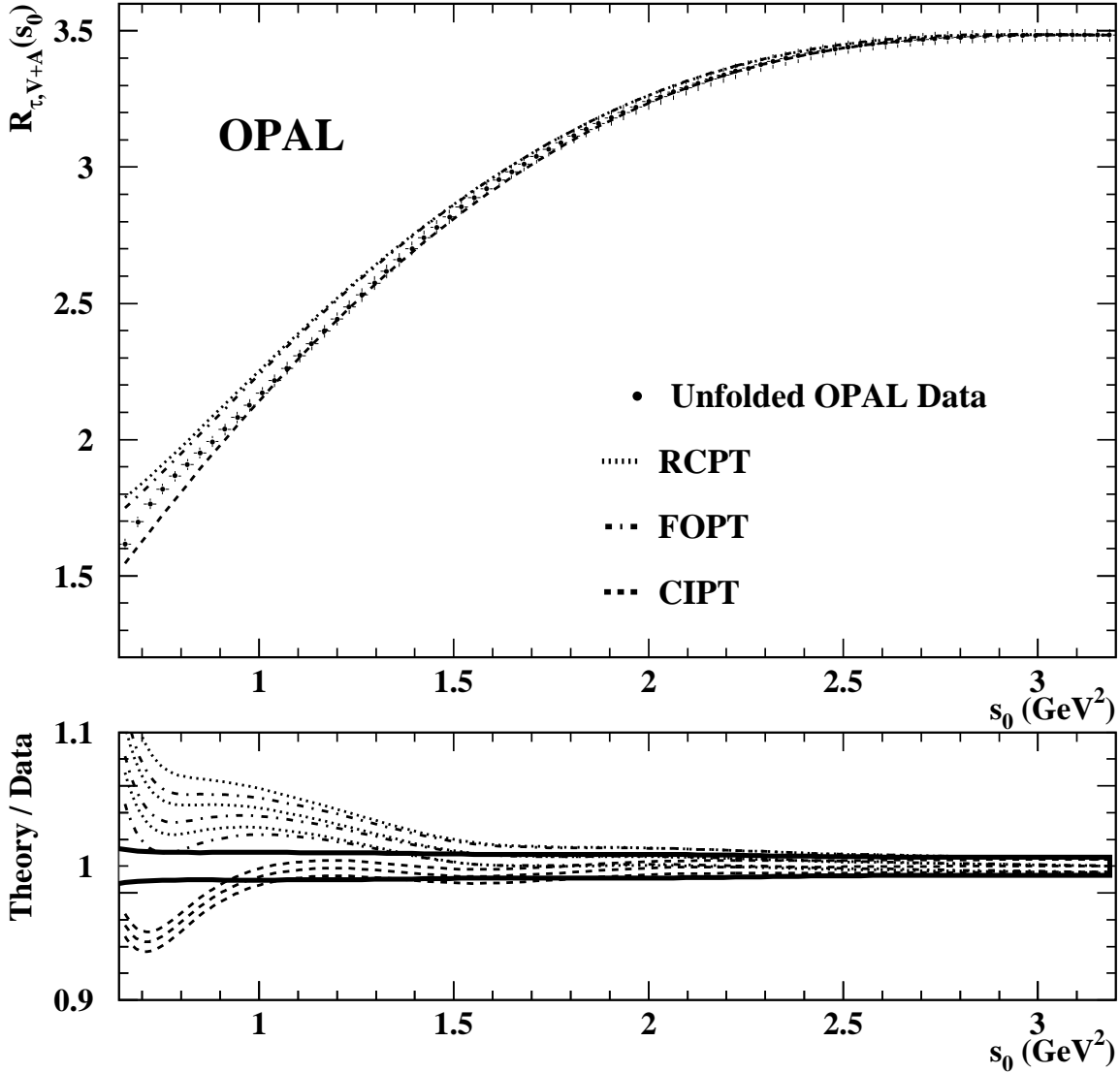$$\alpha_{\mathrm{s}}(m_{\mathrm{Z}}^2) = 0.120 \pm 0.003. \tag{34}$$

Figure 7: *The non-strange hadronic decay rate of the τ lepton $R_{\tau,V}(s_0) + R_{\tau,A}(s_0)$ versus the upper integration limit s_0. The points in the upper plot denote OPAL data; the dashed, dashed-dotted and dotted curves represent the theoretical predictions of the three theories with the results from the fit to the moments at $s_0 = m_\tau^2$ used as input. The lower plot shows the three theories normalized to the data. The three sets of dashed, dashed-dotted and dotted curves indicate central values and total experimental errors for each of the three theories. The errors on the data are shown as solid curves.*

theory	observable	value	contributing errors				χ^2/d.o.f.
			data	B	syst.	theo.	
CIPT	$\alpha_{\mathrm{s}}(m_\tau^2)$	0.347	±0.001	±0.012	±0.002	±0.019	0.63/4
	$\langle\frac{\alpha_{\mathrm{s}}}{\pi}GG\rangle/\mathrm{GeV}^4$	0.001	±0.003	±0.006	±0.003	±0.004	
	δ_{V}^6	0.0256	±0.0017	±0.0024	±0.0017	±0.0006	
	δ_{V}^8	-0.0080	±0.0010	±0.0007	±0.0005	±0.0002	
	δ_{A}^6	-0.0197	±0.0016	±0.0022	±0.0019	±0.0010	
	δ_{A}^8	0.0041	±0.0012	±0.0013	±0.0008	±0.0002	
FOPT	$\alpha_{\mathrm{s}}(m_\tau^2)$	0.323	±0.001	±0.008	±0.002	±0.014	0.62/4
	$\langle\frac{\alpha_{\mathrm{s}}}{\pi}GG\rangle/\mathrm{GeV}^4$	0.017	±0.003	±0.004	±0.003	±0.010	
	δ_{V}^6	0.0271	±0.0017	±0.0025	±0.0018	±0.0056	
	δ_{V}^8	-0.0085	±0.0010	±0.0007	±0.0005	±0.0012	
	δ_{A}^6	-0.0183	±0.0016	±0.0023	±0.0019	±0.0052	
	δ_{A}^8	0.0036	±0.0011	±0.0012	±0.0008	±0.0011	
RCPT	$\alpha_{\mathrm{s}}(m_\tau^2)$	0.305	±0.001	±0.007	±0.001	±0.011	0.61/4
	$\langle\frac{\alpha_{\mathrm{s}}}{\pi}GG\rangle/\mathrm{GeV}^4$	0.002	±0.003	±0.005	±0.003	±0.001	
	δ_{V}^6	0.0202	±0.0018	±0.0033	±0.0018	±0.0009	
	δ_{V}^8	-0.0075	±0.0010	±0.0008	±0.0005	±0.0002	
	δ_{A}^6	-0.0252	±0.0017	±0.0032	±0.0020	±0.0006	
	δ_{A}^8	0.0047	±0.0012	±0.0013	±0.0008	±0.0001	

Table 8: *The fit result for α_s and the power corrections from the combined fit to vector and axial-vector moments. The given errors correspond to the data statistics, the uncertainty due to the errors on the branching ratios B, a systematic error from the Monte Carlo statistics, the energy scale, the momentum scale, and the unfolding, and a total theoretical uncertainty.*

10 Measurement of dimension 6 and 8 operators

The results from fit 2 where the separate moments of the vector current and axial-vector current are used are given in table 8. In contrast to α_{s} where the error is dominated by the theoretical uncertainties, the power corrections are almost independent of the theoretical uncertainties for CIPT and RCPT. As mentioned in section 9, this is not the case for the FOPT fit which leads to theoretical errors of the order of (or even larger than) the experimental errors. Due to the correlated unfolding of vector and axial-vector spectra a strong positive correlation between the power corrections of the vector and axial vector current of the same dimension is observed. The power corrections of different dimension but for the same current are anti-correlated. All correlations of the fit parameters for CIPT are summarized in table 9. The fitted values of the strong coupling constant in both fits are in excellent agreement for all three models. The experimental error on α_{s} from this fit is larger than in fit 1 as the additional information from the τ lifetime and the branching ratio $B(\tau \to \mu\nu_\mu\nu_\tau)$ is omitted. Using equation (28), the separate and total power corrections are also in good agreement for all three models. As in fit

	$\alpha_{\mathrm{s}}(m_\tau^2)$	$\left\langle \frac{\alpha_{\mathrm{s}}}{\pi}GG \right\rangle$	δ_{V}^6	δ_{A}^6	δ_{V}^8
$\left\langle \frac{\alpha_{\mathrm{s}}}{\pi}GG \right\rangle$	-57				
δ_{V}^6	-55	99			
δ_{A}^6	-61	96	96		
δ_{V}^8	41	-92	-90	-84	
δ_{A}^8	42	-87	-86	-77	89

Table 9: *Correlations between the QCD parameters from the fit to the moments of the vector and axial-vector current in percent. The given numbers are taken from the CIPT fit result.*

1 all three theories give similar χ^2 values in the fit to the exclusive moments. The theoretical uncertainties behave similarly in fit 1 and fit 2. The sum of all power corrections $\delta_{\mathrm{non\text{-}pert,V/A}}$ and $\delta_{\mathrm{non\text{-}pert,V+A}}$ to $R_{\tau,\mathrm{V/A}}$ and $R_{\tau,\mathrm{V}} + R_{\tau,\mathrm{A}}$ including the dimension 2 quark-mass correction and the dimension 4 correction obtained from the fitted gluon condensate are:

$$\delta_{\mathrm{non\text{-}pert,V}} = \begin{array}{ll} 0.0172 \pm 0.0026 & \mathrm{CIPT} \\ 0.0187 \pm 0.0054 & \mathrm{FOPT} \\ 0.0124 \pm 0.0033 & \mathrm{RCPT,} \end{array} \tag{35}$$

$$\delta_{\mathrm{non\text{-}pert,A}} = \begin{array}{ll} -0.0219 \pm 0.0026 & \mathrm{CIPT} \\ -0.0204 \pm 0.0050 & \mathrm{FOPT} \\ -0.0266 \pm 0.0032 & \mathrm{RCPT,} \end{array} \tag{36}$$

$$\delta_{\mathrm{non\text{-}pert,V+A}} = \begin{array}{ll} -0.0024 \pm 0.0025 & \mathrm{CIPT} \\ -0.0009 \pm 0.0051 & \mathrm{FOPT} \\ -0.0071 \pm 0.0031 & \mathrm{RCPT,} \end{array} \tag{37}$$

where the errors include experimental and theoretical uncertainties. Thus all three theories lead to non-perturbative corrections to $R_{\tau,\mathrm{V}}$ ($R_{\tau,\mathrm{A}}$) of the order 1.6 % (-2.3 %), while a large cancellation of both contributions leads to a total non-perturbative correction to $R_{\tau,\mathrm{V}} + R_{\tau,\mathrm{A}}$ which is compatible with zero and therefore allows a precise measurement of the strong coupling constant in fit 1. The numbers in table 8 can be compared to the estimates given in [4]:

$$\begin{aligned} \left\langle \frac{\alpha_{\mathrm{s}}}{\pi}GG \right\rangle / \mathrm{GeV}^4 &= 0.02 \pm 0.01, \\ \delta_{\mathrm{V}}^6 &= 0.024 \pm 0.013, \\ \delta_{\mathrm{A}}^6 &= -0.038 \pm 0.020, \\ \delta_{\mathrm{V/A}}^8 &\simeq -0.0001. \end{aligned} \tag{38}$$

Only the power corrections of dimension 8 seem to be underestimated, while the other estimates are in good agreement with the measured values. Figure 8 shows the two power corrections of dimension 6 (CIPT) together with the theoretical prediction given in [4].
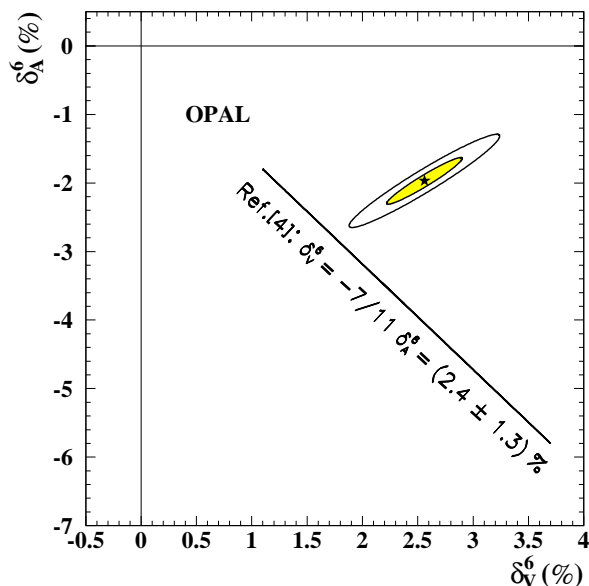
Figure 8: *The power corrections of dimension 6 to $R_{\tau,V/A}$. Shown are the one and two standard deviation contours of the correlated result for the vector and axial-vector current (CIPT) including experimental and theoretical uncertainties. The solid line indicates the theoretical prediction given in [4].*

11 Test of the 'running' of α_s

The fit to the sum of vector and axial-vector moments (fit 1) can be extended to lower values of s_0, thus giving a correlated measurement of the strong coupling at different scales. Four equidistant values for s_0 between $1.3\,\mathrm{GeV}^2$ and m_τ^2 are used. In addition to the five moments at $s_0 = m_\tau^2$ the integrated differential decay rate $R_{\tau,V}^{00}(s_0) + R_{\tau,A}^{00}(s_0)$ for each additional s_0 value is included in the fit (see figure 7).

For the extraction of the 'running' of α_s the number of fit parameters is increased to include the strong coupling $\alpha_s(s_0)$ for each s_0 value below m_τ^2. The result can be examined with the four-loop β-function. This is shown in figure 9, where the β-function has been refitted for all three sets of α_s values. The values at $s_0 = 1.3\,\mathrm{GeV}^2$ were not included in the fit. A comparison of these values with the predicted 'running' shows good agreement in case of CIPT, while a weaker 'running' as predicted by the β-function is preferred by the FOPT and the RCPT values.

Figures 7 and 9 can be regarded as tests of the validity of the OPE for s_0 values below m_τ^2. It has been questioned if the definition of $R_\tau(s_0)$ is still valid in this region [4], since the endpoint $s = s_0$ is no longer suppressed by the $(1-s/m_\tau^2)^2$ term in front of the spectral function (see equation (1)). By defining the hadronic decay rate for a hypothetical τ' with a mass of $m_{\tau'} = \sqrt{s_0}$ and inserting $m_{\tau'}$ for m_τ in equation (1) one gets [8]:

$$R_{\tau',V/A}(s_0) = 12\pi S_{\mathrm{EW}} |V_{\mathrm{ud}}|^2 \int_0^{s_0} \frac{\mathrm{d}s}{s_0} \left(1 - \frac{s}{s_0}\right)^2 \left[\left(1 + 2\frac{s}{s_0}\right) \mathrm{Im}\Pi_{V/A}^{(1)}(s) + \mathrm{Im}\Pi_{V/A}^{(0)}(s)\right], \quad (39)$$

obeying the same quadratic suppression of the endpoint on the real s-axis as $R_{\tau,V/A}(m_\tau^2)$. Figure 10 shows the sum $R_{\tau',V}(s_0) + R_{\tau',A}(s_0)$ versus the upper integration limit s_0. The error
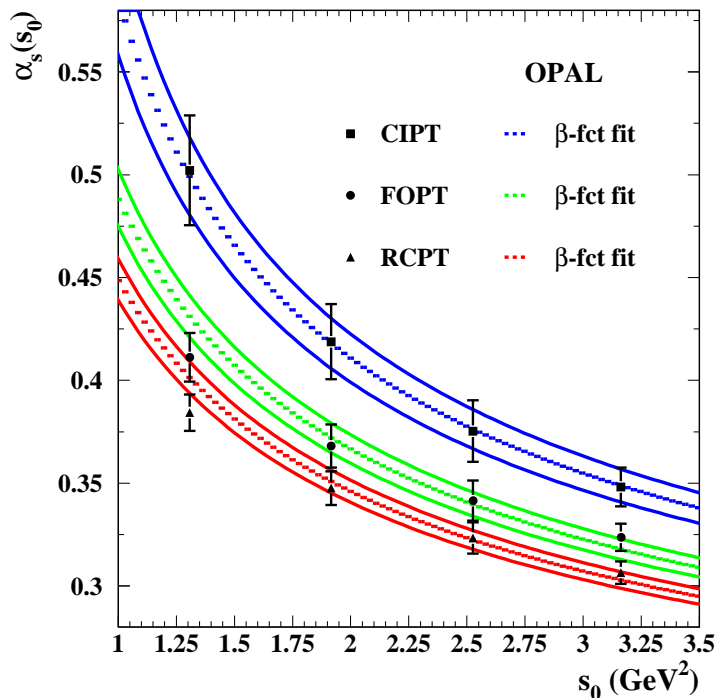
Figure 9: *The 'running' of the strong coupling. The three sets of α_s values are shown as data points. The error bars include statistical and systematic uncertainties. The dashed curves represent the predictions of the 4-loop β-function obtained from fits to the three sets of α_s values not including the values $\alpha_s(1.3\ GeV^2)$. The solid lines depict the errors from the fits.*

band for CIPT in the lower plot shows that the uncertainties increase below $s_0 \simeq 1.5\,\mathrm{GeV}^2$ compared to the error in the lower plot of figure 7. While the error on $R_\tau(s_0)$ is dominated by the uncertainty of the perturbative expansion, the error on $R_{\tau'}(s_0)$ originates mainly from its dependency on the non-perturbative parts. In contrast to R_τ where these power corrections stay constant for all s_0 (see equation (11)) they increase with powers of $1/s_0$ as s_0 decreases in the case of $R_{\tau'}$. As the errors are large for small values of s_0 little can be said about this region.

12   QCD sum rules

Weighted integrals over the difference of the two measured spectral functions shown in figure 6 can be compared to the chiral predictions of QCD sum rules:

$$I_1(s_0) \;=\; \frac{1}{4\pi^2} \int_0^{s_0} \mathrm{d}s\ (v(s) - a(s)) = f_\pi^2, \tag{40}$$

$$I_2(s_0) \;=\; \frac{1}{4\pi^2} \int_0^{s_0} \mathrm{d}s\, s\ (v(s) - a(s)) = 0, \tag{41}$$

$$I_3(s_0) \;=\; \frac{1}{4\pi^2} \int_0^{s_0} \frac{\mathrm{d}s}{s}\ (v(s) - a(s)) = f_\pi^2\, \frac{\langle r_\pi^2 \rangle}{3} - F_{\mathrm{A}}, \tag{42}$$
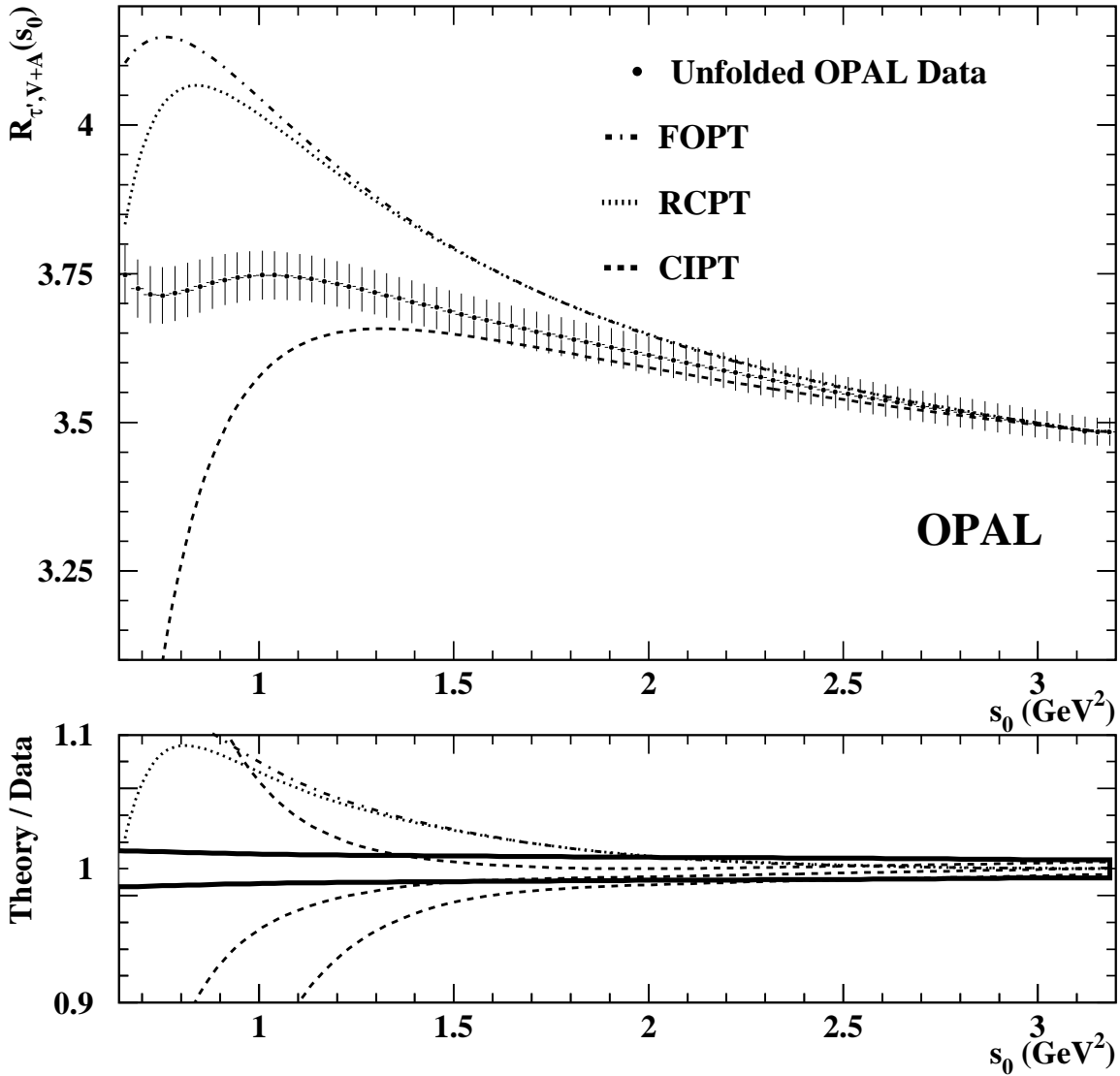
Figure 10: *The non-strange hadronic decay rate of a hypothetical τ' lepton with $m^2_{\tau'} = s_0$ versus the upper integration limit s_0. The points in the upper plot denote OPAL data; the dashed, dashed-dotted and dotted curves represent the theoretical predictions of the three theories with the results from the fit to the moments at $s_0 = m^2_\tau$ used as input. The lower plot shows the three theories normalized to the data. The three dashed curves indicate central values and total experimental errors for CIPT. The dashed-dotted and dotted curves show central values for FOPT and RCPT. The errors for FOPT and RCPT are similar to the CIPT errors and omitted from the plot. The errors on the data are shown as solid lines.*
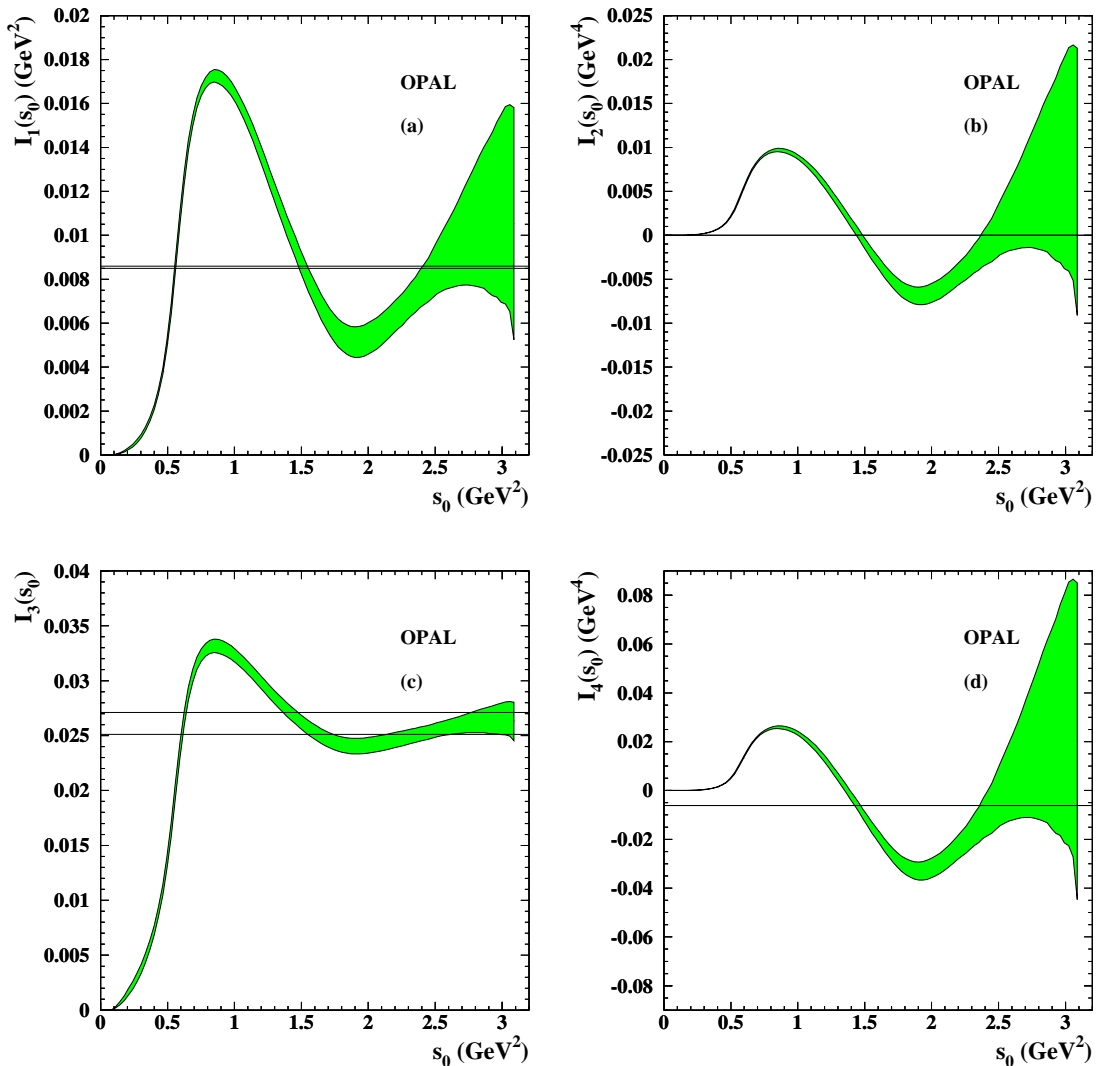
Figure 11: *QCD sum rules. Equations (40)–(43) are shown in the plots (a)–(d). Shown are the integrals versus the upper integration limit as shaded bands. The chiral prediction is given by the lines ($\pm 1\,\sigma$ when two lines are present).*

$$I_4(s_0) \;\; = \;\; \frac{1}{4\pi^2} \int\limits_0^{s_0} \mathrm{d}s \, s \ln\frac{s}{\lambda^2} \, (v(s) - a(s)) = -\frac{4\pi f_\pi^2}{3\,\alpha} \left(m_{\pi^\pm}^2 - m_{\pi^0}^2 \right). \tag{43}$$

Here the right hand side of each equation is understood to be the chiral prediction in the limit $s_0 \to \infty$. Equation (40) is known as the first Weinberg sum rule [52], assuming that the only scalar contribution is given by the pion pole which is related to the pion decay constant $f_\pi = (92.4 \pm 0.26)\,\mathrm{MeV}$ [11]. The second Weinberg sum rule [52] is given in equation (41). The Das–Mathur–Okubo (DMO) sum rule [53] is given by equation (42). Its asymptotic prediction is a function of the pion decay constant f_π, the mean square of the pion charge radius $\langle r_\pi^2 \rangle = (0.439 \pm 0.008)\,\mathrm{fm}^2$ [54] and the axial-vector form factor of the pion $F_\mathrm{A} = 0.0058 \pm 0.0008$ [11][7], and equation (43) gives the electromagnetic mass difference of pions [55]. Note that equation (43) does not depend on the cut-off value λ by virtue of the second Weinberg sum rule.

---

[7]Our definitions of F_A and f_π^2 differ by a factor of $1/2$ from those given in [11]

The saturation of these four sum rules is tested taking into account the full correlations between the measured spectral functions. The plots of figure 11 show the measured values of the integrals I_1-I_4 as error bands including all experimental uncertainties versus the upper integration limit. The asymptotic predictions are drawn as thin lines denoting the present $\pm 1\,\sigma$ ranges.

All four sum rules appear to be saturated at the τ-mass scale within their errors. However, due to the small phase space near the τ-mass which appears in the denominator of the spectral functions these errors are very large except for the DMO sum rule where the $1/s$ factor suppresses the high energy tail. The value of equation (42) at $s_0 = m_\tau^2$ is:

$$I_3(m_\tau^2) = (26.3 \pm 1.8) \cdot 10^{-3}, \tag{44}$$

where the error covers all experimental uncertainties.

12.1 Pion polarizability

Assuming that the DMO sum rule shown in figure 11 (c) is already saturated at the τ-mass scale, its value can be used to predict the electric polarizability of the charged pion as proposed in [56]:

$$\alpha_E = \frac{\alpha}{m_{\pi^\pm}} \left(\frac{\langle r_\pi^2 \rangle}{3} - \frac{I_3}{f_\pi^2} \right). \tag{45}$$

Using the result from the previous section for the DMO sum rule (equation (44)) one gets:

$$\alpha_E = (2.71 \pm 0.88) \cdot 10^{-4}\,\text{fm}^3, \tag{46}$$

which is in good agreement with the value $\alpha_E = (2.64 \pm 0.36) \cdot 10^{-4}\,\text{fm}^3$, derived in [56].

13 Summary

Measurements of the spectral functions of the vector current and the axial-vector current and their applications in QCD have been presented. Within the framework of the Operator Product Expansion, a simultaneous determination of the strong coupling constant α_s and non-perturbative correction terms has been performed. The sum of $R_{\tau,V}$ and $R_{\tau,A}$ was found to involve a large cancellation of the non-perturbative terms and thus has been used together with the τ lifetime and the branching ratio $B(\tau \to \mu\nu_\mu\nu_\tau)$ to give a precise measurement of the strong coupling constant. CIPT has led to the value

$$\alpha_s(m_\tau^2) = 0.348 \pm 0.009_{\text{exp}} \pm 0.019_{\text{theo}},$$

at the τ-mass scale and

$$\alpha_s(m_Z^2) = 0.1219 \pm 0.0010_{\text{exp}} \pm 0.0017_{\text{theo}}$$

at the Z^0-mass scale, where the first error stems from the experimental uncertainties and the second error originates from the theoretical uncertainties. The values obtained for $\alpha_s(m_Z^2)$ using FOPT or RCPT are 2.3 % and 4.1 % smaller, respectively.

The total amount of non-perturbative corrections to $R_{\tau,V}$ ($R_{\tau,A}$) was found to be (1.6 ± 0.4) % $((-2.3 \pm 0.4)$ %), while the correction on the sum of $R_{\tau,V}$ and $R_{\tau,A}$ due to non-perturbative

QCD is found to be only $(-0.3 \pm 0.4)\,\%$. Here the errors include all experimental and theoretical uncertainties.

Assuming the validity of the Operator Product Expansion for energy scales below the τ mass a test of the 'running' of the strong coupling between $s_0 \simeq 1.3\,\mathrm{GeV}^2$ and $s_0 = m_\tau^2$ has been performed. A good agreement between the predicted 'running' from the 4-loop β-function and the fitted α_s values has been observed for CIPT.

The saturation of QCD sum rules at the τ-mass scale has been tested, yielding a measurement of the pion polarizability of $\alpha_\mathrm{E} = (2.71 \pm 0.88) \cdot 10^{-4}\,\mathrm{fm}^3$ as determined from the DMO sum rule.

Acknowledgements

References

[1] E. Braaten, Phys. Rev. Lett. **60** (1988) 1606.

[2] E. Braaten, Phys. Rev. **D39** (1989) 1458.

[3] S. Narison and A. Pich, Phys. Lett. **B211** (1988) 183.

[4] E. Braaten, S. Narison, and A. Pich, Nucl. Phys. **B373** (1992) 581.

[5] F. Le Diberder and A. Pich, Phys. Lett. **B286** (1992) 147.

[6] P.N. Burrows, **MIT-LNS-97-272** (1997), Invited talk at 17th International Conference on Physics in Collision, Bristol (1997).

[7] ALEPH Collaboration, D. Buskulic et al., Phys. Lett. **B307** (1993) 209.

[8] ALEPH Collaboration, R. Barate et al., **CERN-EP-98-012** (1998).

[9] CLEO Collaboration, T. Coan et al., Phys. Lett. **B356** (1995) 580.

[10] W.J. Marciano and A. Sirlin, Phys. Rev. Lett. **61** (1988) 1815.

[11] Particle Data Group, R.M. Barnett et al., Phys. Rev. **D54** (1996) 1, and 1997 off-year partial update for the 1998 edition available on the PDG WWW pages (URL: http://pdg.lbl.gov/).

[12] F. Le Diberder and A. Pich, Phys. Lett. **B289** (1992) 165.

[13] E. Braaten and C.S. Li, Phys. Rev. **D42** (1990) 3888.

[14] T. van Ritbergen, J.A.M. Vermaseren, and S.A. Larin, Phys. Lett. **B400** (1997) 379.

[15] M. Neubert, Nucl. Phys. **B463** (1996) 511.

[16] C.N. Lovett-Turner and C.J. Maxwell, Nucl. Phys. **B452** (1995) 188.

[17] C.J. Maxwell and D.G. Tonge, Nucl. Phys. **B481** (1996) 681.

[18] K.G. Chetyrkin, A.L. Kataev, and F.V. Tkachev, Phys. Lett. **B85** (1979) 277.

[19] M. Dine and J. Sapirstein, Phys. Rev. Lett. **43** (1979) 668.

[20] W. Celmaster and R.J. Gonsalves, Phys. Rev. Lett. **44** (1980) 560.

[21] S.G. Gorishnii, A.L. Kataev, and S.A. Larin, Phys. Lett. **B259** (1991) 144.

[22] L.R. Surguladze and M.A. Samuel, Phys. Rev. Lett. **66** (1991) 560, Erratum: ibid. **66** (1991) 2416.

[23] A. Pich, **FTUV-97-03** (1996), Invited talk at 20th Johns Hopkins Workshop on Current Problems in Particle Theory, Heidelberg (1996).

[24] A.L. Kataev and V.V. Starshenko, Mod. Phys. Lett. **A10** (1995) 235.

[25] K.G. Wilson, Phys. Rev. **179** (1969) 1499.

[26] M.A. Shifman, A.I. Vainshtein, and V.I. Zakharov, Nucl. Phys. **B147** (1979) 385.

[27] M.A. Shifman, A.I. Vainshtein, and V.I. Zakharov, Nucl. Phys. **B147** (1979) 448.

[28] M.A. Shifman, A.I. Vainshtein, and V.I. Zakharov, Nucl. Phys. **B147** (1979) 519.

[29] OPAL Collaboration, K. Ahmet et al., Nucl. Instrum. Methods **A305** (1991) 275.

[30] P. Allport et al., Nucl. Instrum. Methods **A324** (1993) 34.

[31] P. Allport et al., Nucl. Instrum. Methods **A346** (1994) 476.

[32] M. Hauschild et al., Nucl. Instrum. Methods **A314** (1992) 74.

[33] S. Jadach, B.F.L. Ward, and Z. Wąs, Comp. Phys. Comm. **79** (1994) 503.

[34] S. Jadach, Z. Wąs, R. Decker, and J.H. Kühn, Comp. Phys. Comm. **76** (1993) 361.

[35] R. Brun et al., **CERN-DD/EE/84-1** (1989).

[36] J. Allison et al., Nucl. Instrum. Methods **A317** (1992) 47.

[37] T. Sjöstrand, Comp. Phys. Comm. **82** (1994) 74.

[38] M. Bohm, A. Denner, and W. Hollik, Nucl. Phys. **B304** (1988) 687.

[39] F.A. Beerends, R. Kleiss, and W. Hollik, Nucl. Phys. **B304** (1988) 712.

[40] R. Battacharya, J. Smith, and G. Grammer, Phys. Rev. **D15** (1977) 3267.

[41] J. Smith, J.A.M. Vermaseren, and G. Grammer, Phys. Rev. **D15** (1977) 3280.

[42] OPAL Collaboration, R. Akers et al., Phys. Lett. **B328** (1994) 207.

[43] OPAL Collaboration, J. Allison et al., Z. Phys. **C66** (1995) 31.

[44] G.A. Akopdjanov et al., Nucl. Instrum. Methods **140** (1977) 441.

[45] V. Blobel, **DESY-84/118** (1984), Lectures given at 1984 CERN School of Computing, Aiguablava.

[46] OPAL Collaboration, K. Ackerstaff et al., Z. Phys. **C75** (1997) 593.

[47] J.H. Kühn and A. Santamaria, Z. Phys. **C48** (1990) 445.

[48] Y. Tsai, Phys. Rev. **D4** (1971) 2821.

[49] M. Girone and M. Neubert, Phys. Rev. Lett. **76** (1996) 3061.

[50] G. Rodrigo, A. Pich, and A. Santamaria, Phys. Lett. **B424** (1998) 367.

[51] LEP Collaborations ALEPH, DELPHI, L3, OPAL, LEP Electroweak Working Group and SLD Heavy Flavor Group, D. Abbaneo et al., **CERN-PPE-97-154** (1997).

[52] S. Weinberg, Phys. Rev. Lett. **18** (1967) 507.

[53] T. Das, V.S. Mathur, and S. Okubo, Phys. Rev. Lett. **19** (1967) 859.

[54] NA7 Collaboration, S.R. Amendolia et al., Nucl. Phys. **B277** (1986) 168.

[55] T. Das, G.S. Guralnik, V.S. Mathur, F.E. Low, and J.E. Young, Phys. Rev. Lett. **18** (1967) 759.

[56] V. Kartvelishvili, M. Margvelashvili, and G. Shaw, Nucl. Phys. Proc. Suppl. **A54** (1997) 309.